

Quantifying Perovskite Solar Cell Degradation via Machine Learning from Spatially Resolved Multimodal Luminescence Time Series

Giulio Barletta^{1,†}, Simon Ternes^{2,†}, Saif Ali², Zohair Abbas², Chiara Ostendi², Marialucìa D’Addio², Erica Magliano², Pietro Asinari^{1,3}, Eliodoro Chiavazzo^{1,*}, Aldo Di Carlo^{2,4,**}

¹ *Department of Energy, Politecnico di Torino, Corso Duca degli Abruzzi, 24, Torino, 10129, Italy*

² *CHOSE—Centre for Hybrid and Organic Solar Energy, University of Rome Tor Vergata, Via del Politecnico, 1, Rome, 00133, Italy*

³ *INRIM, Istituto Nazionale di Ricerca Metrologica, Strada delle Cacce, 91, Torino, 10135, Italy*

⁴ *ISM-CNR, Institute of Structure of Matter, Consiglio Nazionale delle Ricerche, Via Fosso del Cavaliere, 100, Rome, 00133, Italy*

Abstract

Perovskite solar cells (PSCs) have rapidly gained in power conversion efficiency (PCE) within the last 15 years, providing a promising alternative or add-on to established silicon semiconductors for future’s large-scale photovoltaic (PV) deployment. Yet, besides scalability of fabrication routines, operational stability remains a key bottleneck for commercial roll-out of perovskite based PV. In this context, reliable and fast assessment of the state of health and degradation mechanisms that is compatible with field deployment are of utmost importance. Electrical diagnostics such as current–voltage (J–V) sweeps under illumination provide accurate performance metrics but are time-consuming and do not resolve spatially localized degradation, motivating non-invasive imaging-based alternatives. Here, we present a deep-learning framework to estimate PSC efficiency retention $R_{\text{PCE}} = \text{PCE}_t / \text{PCE}_0$ directly from multimodal luminescence imaging acquired during device aging, and we demonstrate that leveraging spatially resolved luminescence patterns may reveal key to improving prediction performance and robustness compared to intensity-only baselines. In our approach, each learning sample consists of electroluminescence (EL), open-circuit photoluminescence (PL_{oc}), and short-circuit photoluminescence (PL_{sc}) acquired at an aged state together with device-specific reference images at $t = 0$, enabling the model to learn degradation-relevant spatial changes relative to the initial condition. These data were acquired over a time span of 5–70 h in an automated, house-built measurement platform. We introduce LumPerNet, a compact convolutional neural network that regresses R_{PCE} from stacked multimodal image tensors, and benchmark it against an intensity-only baseline multilayer perceptron regressor. Using a leakage-aware evaluation protocol with device-level held-out testing and four-fold cross-validation, and restricting analysis to the operational window $R_{\text{PCE}} \in [0.8, 1.2]$, LumPerNet achieves a substantially higher and more robust performance (MAE: –23.4%, RMSE: –25.6%, R^2 : +0.417) with respect to the intensity-only baseline, confirming that spatially resolved EL/PL patterns carry predictive information beyond global luminescence decay. To quantify the role of multimodality, we further perform an exhaustive modality ablation study over all single- and paired-modality inputs. We find that multimodal training yields the best generalization, while carefully chosen bimodal configurations can retain most of the full-model performance, whereas other pairings can be unstable across device splits, highlighting that complementary physical contrast, rather than channel count, governs robustness. Representative device trajectories further show temporally coherent R_{PCE} estimates and uncertainty quantification via model ensembling. Overall, this work establishes a reproducible pipeline linking automated luminescence imaging to electrical R_{PCE} labels, and positions spatially resolved imaging as a practical route for accelerated stability testing and non-invasive degradation monitoring in perovskite photovoltaics.

Keywords: Artificial Intelligence, Machine Learning, Perovskite, Photovoltaics, Luminescence Imaging, Degradation Diagnostics, Efficiency Retention

[†] Authors contributed equally

1. Introduction

Perovskite solar cells (PSCs) have emerged as one of the most promising emerging photovoltaic (PV) technologies [1–6], achieving a remarkable leap in power conversion efficiency (PCE), from around 3.8% in 2009 to over 27% for single junction PSCs [7, 8] at the time of writing. Furthermore, the flexible bandgap of perovskite absorber thin films has enabled their deployment in the tandem device architecture, yielding 34.85% for perovskite–Si tandem cells [9], and 30.1% for perovskite–perovskite tandem cells in 2025 [10]. Despite these performance milestones, their medium- to long-term operational stability remains a critical challenge, with reports demonstrating stable operation on the order of 10^3 h under standardized stress protocols, although full T_{80} values are not always reached or consistently reported [11–14]. Unlike silicon PV, which have demonstrated moderate degradation over three decades defining the industry standard [15–17], PSCs are highly sensitive to environmental stressors such as moisture, oxygen, UV light, and thermal cycling. On the short to medium timescale (up to 10^2 h), the performance of perovskite based PV was shown to fluctuate according to mostly reversible transient effects such as light soaking and path dependence [18, 19]. However, on the medium to long timescale ($> 10^2$ h), irreversible degradation of the perovskite crystal structure to lead halide (rich) phases is routinely observed [20–23]. This instability is mediated by intrinsic material vulnerabilities (including phase transitions, ion migration, and interfacial degradation) as well as extrinsic factors like poor encapsulation and crystallographic defects [12, 13, 20, 24–27].

While stability has historically been one of the main barriers for perovskite PV, recent years have witnessed significant progress toward addressing these limitations: for instance, early outdoor field trials have demonstrated stable operation despite the technology’s relative youth [28–30]. Furthermore, several studies document thousands of hours of continuous operation under realistic conditions and under standardized stress conditions similar to those applied to silicon [31–35], such as elevated-temperature storage or damp heat (ISOS D2 and D3 elevated stress tests [11, 36]). However, translating these stability advances into rapid iteration and scalable quality control still requires monitoring tools that are faster than repeated full electrical characterization and that can localize where degradation initiates. This motivates non-invasive luminescence imaging as a practical readout for accelerated testing, where data-driven models can translate spatially resolved patterns into device-level performance retention even when the target metric is spatially averaged, as explored in this work.

The operational stability of metal-halide perovskites is governed by coupled chemical and ionic processes that are strongly influenced by the environment and by electrostatic boundary conditions within the device stack [11, 12]. Operational stability drifts can be broadly grouped into reversible (metastable) and irreversible contributions, which may coexist and act on different time scales [11, 37]. A central irreversible failure route is the partial or complete conversion of the perovskite absorber into PbI_2 (and volatile organic species in MA/FA-based compositions), which can be triggered by moisture-assisted hydrolysis and hydrate formation, photo-oxidation in the presence of oxygen, and elevated temperature, each of which perturbs the ionic lattice and facilitates defect formation and ion motion [12, 38]. At the device level, both irreversible and reversible performance changes are closely linked to mobile ionic defects (notably halide-related vacancies and interstitials) that redistribute under illumination and bias, leading to internal field screening, interfacial ion accumulation, and time-dependent changes in recombination, hysteresis, and apparent performance [11, 39]. In mixed-halide compositions, ionic redistribution can also manifest as light-induced halide segregation, with partial reversibility upon returning to dark conditions [21]. In addition to degradation, repeated or continuous bias and/or illumination (“light soaking”) can induce temporary performance improvements, often attributed to evolving interfacial electrostatics and contact properties mediated by ionic redistribution rather than permanent bulk passivation [40–42]. Consistently, partial or even near-complete recovery of device performance after dark storage has been widely reported and is commonly referred to as self-healing, highlighting the metastable character of several degradation modes in PSCs [21, 43, 44]. At interfaces, irreversible degradation can be amplified by interfacial redox chemistry and compositional exchange, including electrode- or TCO-related elemental migration into the absorber or transport layers, which can alter band alignment and increase interfacial recombination and contact barriers [12, 20]. Device-level stressors therefore map onto distinct degradation signatures: humidity primarily accelerates chemical decomposition and interfacial reactions [33, 45]; UV and high-energy photons can promote interfacial contact degradation and, in oxide-based architectures, photocatalytic pathways [46–48]; thermal stress and

*eliodoro.chiavazzo@polito.it

**aldo.dicarlo@uniroma2.it

thermal cycling exacerbate diffusion, interconnect weaknesses, and contact non-uniformities [34, 49]; electrical bias can further drive ion accumulation at interfaces and promote irreversible reactions [44, 50, 51].

Recently, the first perovskite-based PV modules have been delivered to customers for pilot deployment by companies including Oxford PV (EU), Swift Solar (US), and Microquanta (China) [52–54]. These advances highlight the accelerating scientific and industrial momentum of perovskite PV. Due to the comparatively young age of the technology, field tests remain on the pilot level and the state of the deployed modules must be closely observed. Nevertheless, the underlying degradation mechanisms governing PSC aging remain fundamentally different from those of silicon and other conventional semiconductors. Therefore, developing robust, non-invasive methods to monitor such degradation and predict the associated performance decline is thus integral to realizing the full potential of PSCs for both laboratory research and utility-scale deployment. Beyond providing a stability figure of merit, monitoring degradation through time enables practical decisions during both development and deployment. For instance, it can (i) support high-throughput screening of materials, interfaces, and encapsulation strategies by rapidly identifying device architectures that develop localized defects, (ii) guide targeted follow-up diagnostics by pinpointing where degradation initiates (e.g., edges, contacts, shunted regions), and (iii) enable automated quality control and early-warning indicators in pilot-scale or field operation, where frequent electrical characterization is impractical.

The standard approach to monitoring PV performance relies on classical electrical characterization techniques such as current–voltage (J–V) curves, external quantum efficiency (EQE), and impedance spectroscopy. While these methods provide accurate and physically interpretable information, they are relatively time-consuming and poorly suited for non-invasive field inspection. Moreover, their lack of spatial resolution prevents the identification of local failure points such as degradation hotspots or shunt pathways. In silicon PV, electroluminescence (EL) and photoluminescence (PL) imaging are now well-established for detecting cracks, shunts, hotspots, and potential-induced degradation, and have been successfully scaled to field-level inspections through drone-based and lock-in techniques [55–57]. Recently, these image-based diagnostic techniques have gained traction as non-invasive tools for detecting and quantifying degradation also in perovskite PV [55, 58–61]. Still, as compared to silicon PV, the use of EL and PL imaging for PSCs remains comparatively underexplored. While PL was extensively used in laboratory studies to probe carrier lifetimes, trap densities, and interfacial recombination [62–66], systematic efforts to link the temporal evolution of luminescence patterns during aging with device degradation are still scarce [67–69]. In contrast, EL imaging of PSCs is less explored due to additional challenges arising from the required electrical injection of charges such as ion migration, contact instability, and inter-device variability, which complicate the interpretation of spatial patterns [61, 70, 71].

Existing machine learning (ML)- driven approaches in PSC diagnostics can be broadly grouped into three classes. First, a large body of work uses EL/PL imaging (often at a single time point) for static characterization tasks, such as defect segmentation [72–75] or inference of electrical parameters and absolute efficiency from spatial patterns [76–80]. Second, complementary ML efforts target lifetime and stability metrics using tabular descriptors of composition, processing, and operating conditions, typically leveraging literature or database-derived labels rather than operando-imaging time series [81–84]. Third, recent studies have begun to exploit time series of optical measurements (including high-throughput or operando luminescence) with data-driven forecasting or self-supervised learning, highlighting the potential of temporal optical signals for monitoring degradation dynamics [85, 86]. Despite these advances, to the best of our knowledge no existing framework combines multimodal EL/PL imaging acquired repeatedly during aging with a leakage-aware evaluation protocol to quantitatively predict a physically interpretable, device-level degradation metric from the temporal evolution of spatial luminescence patterns.

The proposed methodology departs from traditional degradation modeling approaches that are mainly based on empirical extrapolation [87–89] or isolated electrical measurements [90, 91]. Instead, it leverages multimodal time series of luminescence images, combining EL and PL data acquired at both reference and aged states, to train ML models that regress degradation directly from visual data. In this work, we adopt the efficiency retention R_{PCE} , defined as the ratio between the instantaneous and initial PCE

$$R_{\text{PCE}}(t) = \frac{\text{PCE}_{\text{avg}}(t)}{\text{PCE}_{\text{avg}}(t=0)}, \quad (1)$$

as a degradation metric for PSCs. Here, the $\text{PCE}(t)$ is the PCE recorded at time t computed as the average of forward and reverse J–V scans. This quantity is often used in literature as a measure of performance degradation [37, 45, 92]. Although it has been criticized as an absolute measure for degradation studies due to the possibility of hiding prior

degradation in the normalization constant [11, 37, 93], it serves here as the target variable to let all investigated targets start at the same value at $t = 0$ for our predictive framework. By explicitly combining temporal dynamics with complementary luminescence modalities, the framework is designed to provide a non-invasive route for quantifying degradation without explicit electrical measurements at the device terminals.

In detail, we demonstrate, on three representative datasets spanning distinct device architectures, that convolutional neural networks (CNNs) trained on multimodal time series of luminescence images can learn degradation-relevant spatial patterns and predict the efficiency retention of PSCs with sufficient accuracy for reliable monitoring and screening. While EL and PL probe distinct recombination pathways and can respond differently to spatially localized defects, it is not yet clear whether a reduced set of modalities would suffice. We therefore explicitly quantify the benefit of combining EL, PL_{oc} , and PL_{sc} through an exhaustive ablation study over all single- and paired-modality inputs. This work focuses on establishing a general and extensible framework for image-based R_{PCE} prediction, rather than on optimizing predictive accuracy for a specific dataset.

Such an image-driven approach can complement established electrical diagnostics and outperform space-averaged monitoring by exploiting automated, spatially resolved, and scalable monitoring of device aging. Beyond advancing laboratory diagnostics, it could support accelerated stability testing, production-line quality control, and eventually field-level durability screening. More broadly, integrating R_{PCE} prediction with luminescence imaging offers a scalable data-driven approach to monitor and screen degradation in PSCs. While not intended to replace mechanistic models, such tools can guide targeted experimental characterization to elucidate dominant failure mechanisms, a prerequisite for achieving long-term stability in next-generation PV technologies.

This work is structured as follows. Section 2 describes the employed methodology, starting with the description of the experimental automated aging and imaging setup, continuing with the end-to-end dataset construction, from region of interest (ROI)-based pre-processing to R_{PCE} label generation, and ending with the introduction of the cross-validated (CV) training protocol and device-level held-out testing. Section 3 reports quantitative and qualitative results for multimodal image-based R_{PCE} prediction, including the comparison to an intensity-only baseline, and the modality-ablation study. Finally, Section 4 summarizes the main findings, discusses limitations, and outlines directions toward full-lifecycle and deployment-oriented monitoring.

2. Methods

Table 1: Notation used for multimodal luminescence imaging and efficiency-retention prediction.

Symbol	Meaning
t	Aging time (elapsed time since the start of the aging experiment).
0	Reference condition, i.e., data acquired for a specific device at $t = 0$ before aging.
$EL(t)$	Electroluminescence image acquired at aging time t .
$PL_{oc}(t)$	Photoluminescence image acquired at aging time t under open-circuit conditions (oc).
$PL_{sc}(t)$	Photoluminescence image acquired at aging time t under short-circuit conditions (sc).
$r_{EL}(t)$	Pixel-wise ratio channel for EL, defined as $EL(t)/EL(0)$.
$r_{PL_{oc}}(t), r_{PL_{sc}}(t)$	Pixel-wise ratio channels $PL_{oc}(t)/PL_{oc}(0)$ and $PL_{sc}(t)/PL_{sc}(0)$.
$\mathbf{x}(t)$	Stacked multimodal input tensor at time t (see Eq. 3).
$PCE(t)$	Power conversion efficiency measured from indoor J-V at aging time t .
R_{PCE}	Efficiency retention, $R_{PCE} = PCE(t)/PCE(0)$.
\hat{y}	Model prediction of R_{PCE} for a given sample.

2.1. Device fabrication

This work investigates batches of perovskite solar cells with two distinct device Architectures. The first Architecture A, CsFAMA PSCs fabricated by a two-step hybrid (thermal evaporation / solution) process, constitutes the majority of devices in the dataset and was tested in two separate batches, which share the same layer sequence and composition but underwent aging characterization at different times. The second Architecture B, solution-processed

FACs PSCs, is used as a second example to enhance the generalization capability of the employed methodology. In both cases the inverted p-i-n structure is used.

In the dataset bookkeeping, three batch IDs are used: Batch 0 and Batch 1 correspond to Architecture A measured in two independent campaigns, whereas Batch 2 corresponds to Architecture B. In the following, we report the fabrication protocols for Architectures A and B.

2.1.1. Substrate preparation and hole transport layer (HTL) deposition

Fluorine-doped tin oxide (FTO) coated glass for Architecture A and indium tin oxide (ITO) coated glass for Architecture B was cut into $2.5 \times 2.5 \text{ cm}^2$ substrates, which were then patterned by P1 isolation using an ultraviolet picosecond laser, in order to define four independent pixels per substrate. Substrates were sequentially cleaned with detergent solution, deionized water, acetone, and 2-propanol (10 min sonication each), followed by 15 min UV/ozone treatment. The substrates were transferred to a nitrogen filled-glovebox for HTL deposition. $80 \mu\text{L}$ of a 0.5 mg mL^{-1} solution of (4-(3,6-Dimethoxy-9H-carbazol-9-yl)butyl)phosphonic acid (MeO-4PACz) in ethanol for Architecture A or (2-(3,6-Dimethoxy-9H-carbazol-9-yl)ethyl)phosphonic acid (MeO-2PACz) in ethanol for Architecture B were deposited on the glass substrates and, following a 10 s waiting time, spin coated at 5000 rpm for 30 s and then annealed at 100°C for 10 min.

2.1.2. Interlayer, perovskite deposition and passivation for Architecture A

After the HTL deposition, a $80 \mu\text{L}$ of a 0.5 mg mL^{-1} solution of 2-decyl[1]benzothieno[3,2-b][1]benzothiophene (C10-BTBT) in dimethylformamide (DMF) was spin coated at 5000 rpm for 20 s and annealed at 100°C for 5 min.

For the two-step hybrid deposition, the substrates were loaded in a multi-source thermal evaporation system (KE-500K by Kenosistec) integrated within a nitrogen-filled glovebox. The pressure in the chamber was brought to $\sim 10^{-6}$ mbar, a film of PbI_2 and CsBr (with a ratio of 10:1) was thermally co-evaporated onto the substrates. Afterwards, formamidinium iodide (FAI; 0.48 M), methylammonium bromide (MABr; 0.09 M), and methylammonium chloride (MACl; 0.09 M) were dissolved in ethanol and dynamically spin-coated at 4500 rpm for 30 s, in order to form a $\text{Cs}_{0.12}\text{FA}_{0.79}\text{MA}_{0.09}\text{Pb}(\text{I}_{0.85}\text{Br}_{0.15})_3$ perovskite. The samples were then annealed in ambient air, with a controlled humidity in the range 30% – 40%, at 125°C for 25 min. The devices were brought to a dry-air glovebox where a post-treatment was performed by spin coating phenethylammonium chloride (PEACl; 1.5 mg mL^{-1} in ethanol) at 5000 rpm for 30 s and annealing at 100°C for 10 min.

2.1.3. Perovskite deposition and passivation for Architecture B

The perovskite precursor solution ($1.4 \text{ M Cs}_{0.17}\text{FA}_{0.83}\text{Pb}(\text{I}_{0.75}\text{Br}_{0.25})_3$) was prepared in *N,N*-dimethylformamide (DMF) and dimethyl sulfoxide (DMSO) (DMF:DMSO = 4:1 v/v) and stirred overnight at room temperature. The perovskite layer was deposited by spin coating ($100 \mu\text{L}$, 4000 rpm, 35 s); chlorobenzene (CB, $150 \mu\text{L}$) was used as antisolvent during the last 15 s), followed by annealing at 100°C for 20 min. Post-treatment was performed by spin coating phenethylammonium chloride (PEACl; 2 mg mL^{-1} in isopropyl alcohol (IPA)) at 6000 rpm for 30 s and annealing at 100°C for 5 min.

2.1.4. Electron transport layer (ETL), buffer layer, and top contact deposition

The electron transport layer phenyl-C61-butyric-acid-methyl ester (PCBM; 27 mg mL^{-1} in CB:dichlorobenzene (DCB) = 0.75:0.25 v/v, $80 \mu\text{L}$) was deposited by dynamic spin coating at 2000 rpm for 30 s and annealed at 100°C for 5 min. An aluminium-doped zinc oxide (AZO) layer was deposited after PCBM by spin coating as reported in Ref. [94]. A 170 nm ITO top electrode was then sputtered using a Kenosistec KS-400 sputtering system. For Architecture B only, a 100 nm copper layer was deposited by thermal evaporation through a shadow mask which protected the active area of each pixel. Finally, for each pixel, a portion of the positive FTO bottom contact was uncovered by removing the perovskite layer with a 7:1 DMF:xylene solution, and silver paste was applied to both the bottom FTO (or ITO for Architecture B) and top ITO contacts.

2.2. Device aging and monitoring

Stability tests were conducted in a custom-built setup designed to enable controlled degradation of PSCs with automatic integrated temperature control, electrical characterization and luminescence imaging. The experimental

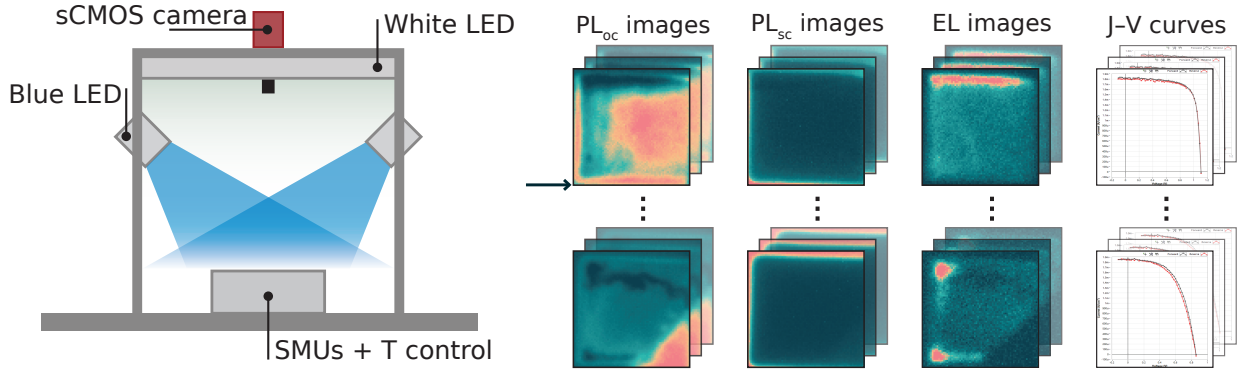


Figure 1: Experimental monitoring workflow and acquired data modalities. A custom chamber integrates temperature control and source-measure units (SMUs) with two illumination channels (white LED for J–V acquisition, blue LED for PL excitation) and an sCMOS camera for spatially resolved imaging. At user-selected aging times, the automated monitoring cycle yields paired PL images at open circuit (PL_{oc}) and short circuit (PL_{sc}), EL images under forward bias (1.5 V), and corresponding J–V curves, forming multimodal time series for each device.

monitoring workflow is summarized in Figure 1, including a schematic of the custom chamber and instrumentation (left) and the resulting multimodal time series acquired at successive aging times (right), namely PL_{oc} , PL_{sc} , EL images, and indoor J–V curves. All hardware components were coordinated through a Raspberry Pi 4 (Ubuntu OS), which managed device communication and task synchronization via Python-based control scripts. The single-board computer issued digital control signals through GPIO pins to drive illumination sources, triggered imaging acquisition over USB 3.0, and interfaced with the electrical characterization and aging platform via its application programming interface (API). Electrical biasing and current-voltage characterization were performed using the Arkeo system (Cicci Research srl), which enabled both J–V measurements and device biasing during luminescence acquisition. Indoor J–V curves were recorded under broadband white illumination provided by a DLP Ring Light (Smart Vision Lights). Note that the white-LED J–V measurements are used to compute relative efficiency retention under consistent indoor illumination rather than to report absolute AM1.5G-certified efficiencies. Unless otherwise stated, all electrical performance metrics reported in this work (V_{oc} , J_{sc} , fill factor (FF), and PCE) refer to these indoor J–V measurements acquired under controlled laboratory illumination. For EL imaging, a forward bias of 1.5 V was applied to inject carriers and induce radiative recombination. For PL imaging, the system sequentially imposed open-circuit and short-circuit conditions while the samples were optically excited by two LSR300 linear light bars (470 nm LEDs, Smart Vision Lights), mounted on aluminum supports to ensure uniform excitation across the devices, mechanical stability, and effective heat dissipation during continuous operation. Normalized emission spectra of the white and blue LED sources, as well as a photograph of the experimental setup, are provided in the Supplementary Information (Figures S1 and S2).

Luminescence images were captured using a Quantalux CS2100M-USB sCMOS camera (Thorlabs) equipped with a FELH0600 long-pass filter ($\lambda_{cut-on} = 600$ nm, Thorlabs) to suppress the excitation light and isolate the emission signal. Camera exposure time and gain were kept constant throughout the test series for each imaging mode to enable quantitative comparison of luminescence intensity. Each image contained up to 32 cells arranged in a fixed layout (see Section 2.3).

Samples under analysis were kept at a constant temperature, controlled through the Arkeo platform and maintained at 30 °C in ambient atmosphere for the proof-of-concept aging series reported herein. The devices were not encapsulated to enable ingress of humidity to increase performance variation during the measurement time (in future measurements, humidity will be exactly controlled and monitored). The temperature was not elevated above 30 °C to prevent photoluminescence quenching. At user-defined time intervals (identical across all batches), the control software executed a fully automated measurement sequence (Figure 2) comprising (i) a J–V sweep under continuous white-LED illumination; (ii) PL imaging under continuous blue LED excitation at open-circuit ($V = V_{oc}$) and short-circuit ($V = 0$ V) conditions; and (iii) EL imaging under forward bias (1.5 V). Within each cycle, all dwell times were kept constant across datasets: 20 s white-light soaking for recombination, 30 s white-light soaking for the J–V sweep, 60 s relaxation at open circuit in the dark to minimize bias-history artifacts, 10 s blue-light soaking for PL_{oc} followed immediately by 10 s for PL_{sc} (i.e., 20 s continuous blue illumination), 15 s dark relaxation at short circuit, and 10 s

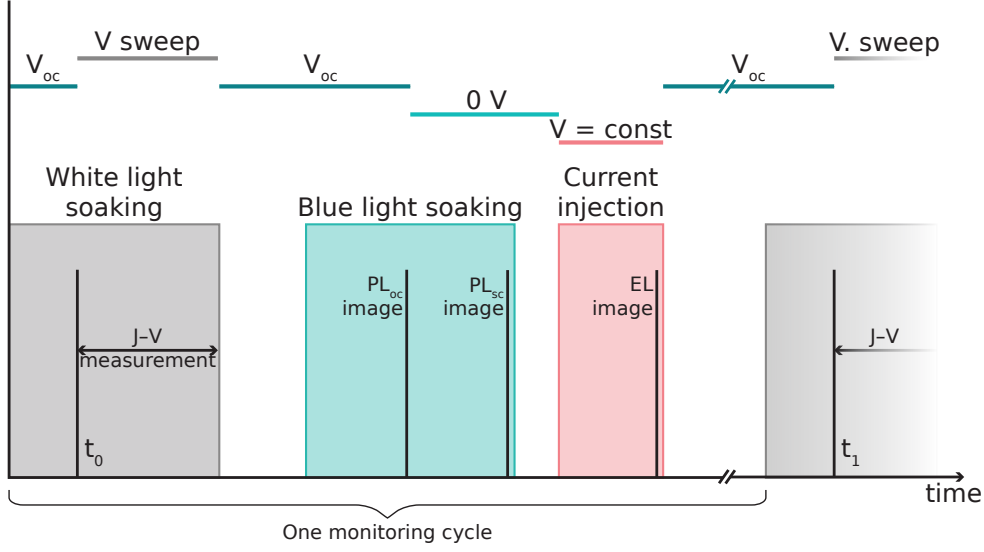


Figure 2: Timing diagram of one automated monitoring cycle executed between two consecutive user-selected aging times, t_0 and t_1 . The cycle comprises (i) white-light soaking (20 s) followed by a J–V sweep under white illumination (30 s); (ii) dark relaxation at open circuit (60 s); (iii) PL imaging under continuous blue illumination at open circuit (PL_{oc} , 10 s) and then immediately at short circuit (PL_{sc} , 10 s; 20 s total blue illumination); (iv) dark relaxation at short circuit (15 s); and (v) EL imaging during forward-bias current injection (10 s). J–V sweeps were performed at every cycle, whereas luminescence images were stored only at a subset of cycles following a progressively sparser schedule at later aging times; the illumination and voltage program of the cycle was otherwise unchanged across all iterations.

voltage bias for EL acquisition. Between cycles, devices were held at open circuit in the dark to allow for device relaxation and self-healing. J–V sweeps were performed at every monitoring cycle, images were stored according to a progressively sparser schedule to balance temporal resolution and acquisition overhead: images were recorded at every iteration for $\#_{iter} \leq 100$, every second iteration for $100 < \#_{iter} \leq 200$, and every fifth iteration for $\#_{iter} > 200$. Importantly, the illumination and bias steps associated with PL/EL were still executed at each cycle even when images were not recorded, thereby preserving identical boundary conditions and minimizing systematic differences between cycles with and without stored images. This cycling routine allowed systematic tracking of device performance and luminescence evolution over aging time. Figure 2 schematically summarizes one full automated measurement cycle, highlighting the temporal sequence of electrical characterization and luminescence imaging steps.

2.3. Data processing & label generation

Raw EL and PL image sequences acquired during the accelerated aging experiments were processed through a dedicated Python pipeline developed in-house. The routine performs dark-field correction, hot-pixel removal, and spatial cropping of each device region of interest (ROI) prior to model training. All operations were implemented in Python 3.12 using NumPy [95], Pandas [96], SciPy [97], Matplotlib [98], and tiffle [99]. Each dataset folder contained time-indexed images from the three luminescence modalities (EL, PL_{oc} , PL_{sc}) acquired under identical spatial framing. A single reference image was used to interactively define all ROIs corresponding to the individual cells tested within the same frame. ROI coordinates were saved as JSON and CSV manifests, enabling reproducible batch processing without further user input. Before cropping, each raw image was corrected for fixed-pattern artifacts through dark-field subtraction, following

$$I_{corr} = I_{raw} - I_{dark}. \quad (2)$$

A static hot-pixel mask was first derived from the dark frame itself to flag persistent defective pixels, while a second adaptive despiking step based on median-absolute-deviation statistics was applied frame-by-frame to suppress transient outliers. Pixels exceeding ten standard deviations above the local median were winsorized rather than replaced outright, preserving image texture while mitigating radiometric spikes [100]. After correction, each ROI was cropped into fixed-size (72×72 px) patches centered on the predefined coordinates. The cropped sub-images were stored

in 16-bit TIFF format within a hierarchical folder structure organized by modality and channel, and a manifest file containing all processing metadata (modality, ROI ID, coordinates, and file paths) was automatically generated.

Raw luminescence and electrical data were processed through a two-stage Python workflow designed to ensure spatial and temporal consistency across all modalities. In the first stage, current–voltage (J–V) logs exported from the Arkeo platform were parsed to extract, for each cell and time step, the forward and reverse power conversion efficiencies ($\text{PCE}_{\text{fw}}, \text{PCE}_{\text{rv}}$) together with the individual factors of the PCE, i.e., $V_{\text{oc}}, J_{\text{sc}}$, and FF. These records were associated with the corresponding EL, PL_{oc} , and PL_{sc} images acquired during the same automated measurement cycles, yielding a unified manifest that maps each image triplet to its electrical response. In the second stage, this manifest was used to assemble per-cell datasets for model training. For each device, the luminescence images recorded at the initial cycle were designated as the reference state ($t = 0$), and all subsequent images were paired with this baseline to form time-ordered sequences. For every time step t , a multimodal tensor was constructed as

$$\mathbf{x}(t) = [\text{EL}(t), \text{PL}_{\text{oc}}(t), \text{PL}_{\text{sc}}(t), \text{EL}(0), \text{PL}_{\text{oc}}(0), \text{PL}_{\text{sc}}(0), r_{\text{EL}}(t), r_{\text{PL}_{\text{oc}}}(t), r_{\text{PL}_{\text{sc}}}(t)] \quad (3)$$

where each $r(t) = I(t)/(I(0) + \varepsilon)$ represents a normalized intensity ratio with a small stabilizing constant $\varepsilon = 10^{-6}$. This structure allows the ML model to access both absolute and relative luminescence information, facilitating the learning of degradation-related spatial changes. Unless otherwise stated, models receive the full multimodal tensor comprising EL, PL_{oc} , and PL_{sc} at both t and $t = 0$, together with the corresponding ratio channels. For the modality-ablation experiments (Section 3.3), we construct single-modality tensors by retaining only the channels associated with one modality (e.g., $\mathbf{x}_{\text{EL}}(t) = [\text{EL}(t), \text{EL}(0), r_{\text{EL}}(0)]$) and discarding the remaining channels.

Because each J–V measurement yields forward- and reverse-scan efficiencies, a single representative value was obtained by averaging the two,

$$\text{PCE}_{\text{avg}}(t) = \frac{1}{2} [\text{PCE}_{\text{fw}}(t) + \text{PCE}_{\text{rv}}(t)], \quad (4)$$

which provides a more robust and direction-independent estimate of device performance. The degradation label was defined as the R_{PCE} , calculated according to Equation 1, representing the fraction of the original performance retained over time. The analysis was restricted to samples with R_{PCE} values in the range 0.8–1.2, corresponding to operational regimes above end-of-life and excluding spikes in the early transient efficiency gains [11, 101–104], while also limiting the regression target to the regime where sample density is sufficient for reliable training. Each sample therefore combines temporally aligned multimodal imaging features with the corresponding quantitative degradation metric, forming a consistent basis for supervised learning of PSC aging. All pre-processing steps preserve the spatial structure of the luminescence patterns and do not involve any learned or adaptive transformations.

2.4. Machine learning framework

The objective of the proposed ML framework is to predict the R_{PCE} of PSCs directly from multimodal luminescence imaging data acquired during device aging. The problem is formulated as a supervised regression task, where each input sample consists of paired reference and current EL, PL_{oc} , and PL_{sc} images, and the target is the corresponding R_{PCE} value derived from electrical measurements. The full workflow, including input modalities, baseline comparison, and the cross-validation protocol used for model selection and evaluation, is summarized in Figure 3.

To exploit both the spatial structure of luminescence patterns and their temporal evolution relative to the initial device state, we adopt a CNN-based architecture [105, 106], hereafter referred to as LumPerNet. The image-based input tensor is initially processed to extract spatial features that encode degradation-related changes in EL and PL intensity distributions. The latent representations produced by the CNN backbone are passed to a final Multilayer Perceptron (MLP) regressor [107], which outputs a scalar estimate of the device R_{PCE} . Importantly, the architecture operates on reference–current image pairs, enabling the model to learn relative changes over aging time rather than absolute intensity levels. The incorporation of batch-level information as an additional input is explored separately as an ablation study and is discussed in the Supplementary Information.

To assess whether the proposed multimodal and spatially resolved approach provides a tangible benefit beyond simple global luminescence trends, a baseline regression model was implemented for comparison. This baseline represents a space-averaged degradation model, consisting of a shallow MLP operating only on mean luminescence intensities (spatial information removed by construction). By discarding spatial information and relying solely on

mean EL and PL signals, the baseline represents a minimal model that captures global intensity decay but is insensitive to localized degradation features.

Model development and benchmarking followed a two-stage protocol designed to prevent information leakage and to enable fair comparisons across architectures. First, the dataset was split at the device level into a training–validation subset ($\sim 80\%$ of total samples) and an independent held-out test subset ($\sim 20\%$ of total samples), with stratification by device batch ID to preserve batch proportions across partitions. The held-out test subset was not accessed during model development and was used only for final evaluation.

Within the training–validation subset, four-fold CV was performed, resulting in four independently trained models for each model architecture; importantly, the same train/validation/test splits were used consistently for both LumPerNet and the baseline regressor, enabling a direct and controlled comparison. After filtering to $R_{\text{PCE}} \in [0.8, 1.2]$, the dataset comprises $N_{\text{cells}} = 59$ devices and $N_{\text{samples}} = 12,258$ paired samples across $N_{\text{batches}} = 3$ device batch IDs (23, 23, and 13 devices per batch, respectively). For all folds, per-channel normalization statistics (mean and standard deviation) were computed on the training split only and then applied to validation and test samples. During training, light geometric data augmentation was applied on-the-fly (small random translations and rotations, identical across all channels of a sample), and target-distribution imbalance within the selected R_{PCE} window was mitigated using weighted random sampling [108]. Reported metrics correspond to the mean and standard deviation of the performance obtained on the held-out test set across the four CV runs. In addition, we also report committee (ensemble) performance obtained by averaging the predictions of the 4 fold-trained models on the pooled test set; these single-number metrics can differ from the mean of per-fold metrics. The same splitting strategy and training and evaluation protocols are reused for all ablations to isolate the impact of input modality. The training of both LumPerNet and the baseline regressor, as well as the creation and handling of the dataset, were implemented in Python 3.12 using NumPy [95] and PyTorch [109].

The comparison between the baseline regressor and the proposed LumPerNet is intended as a proof-of-concept benchmark, aimed at assessing whether spatially resolved multimodal luminescence imaging provides predictive value beyond global intensity trends. A comprehensive exploration of alternative architectures and hyperparameter optimization is left to future work.

3. Results

We test the central hypothesis that spatially resolved EL/PL images improve prediction of the device-level, spatially averaged efficiency retention R_{PCE} beyond what is achievable with space-averaged intensity descriptors. We evaluate efficiency retention prediction on time series of luminescence samples paired with synchronized J–V characterization, where each datapoint comprises steady-state multimodal images (EL, PL_{oc} , PL_{sc}) at an aged state t together with device-specific reference images acquired at $t = 0$, and is labeled with $R_{\text{PCE}}(t)$ as defined in Section 2.3. The analysis is restricted to $R_{\text{PCE}} \in [0.8, 1.2]$, focusing on operational efficiency-retention regimes above end-of-life and excluding early transient efficiency gains. Model development follows the leakage-aware protocol in Section 2.4, comprising a device-level split into training–validation and fixed held-out test subsets and four-fold CV within the training–validation subset; metrics are reported as mean \pm standard deviation on the held-out test set across folds.

3.1. R_{PCE} prediction from multimodal luminescence

We first assess whether a compact CNN-based model (LumPerNet) can regress the device R_{PCE} directly from multimodal luminescence images paired with device-specific reference states. All results in this section refer to the operational window $R_{\text{PCE}} \in [0.8, 1.2]$ and to the evaluation protocol described in Section 2.4 (held-out test set, four-fold CV on the remaining devices, and aggregation across four independently trained models).

Across the held-out test set, LumPerNet achieved a mean absolute error of $\text{MAE} = 0.049 \pm 0.007$, a root-mean-square error of $\text{RMSE} = 0.061 \pm 0.005$, and a coefficient of determination $R^2 = 0.553 \pm 0.077$ (mean \pm standard deviation across the four CV-trained models). These results demonstrate that time series of EL/PL image pairs contain sufficient predictive signal to estimate quantitative R_{PCE} within the operational regime, even under a conservative device-level split designed to prevent leakage from temporally adjacent samples.

Performance was broadly consistent across folds. Table 2 reports the per-fold metrics for both the validation and held-out test sets, together with the corresponding mean \pm standard deviation across the four cross-validation runs,

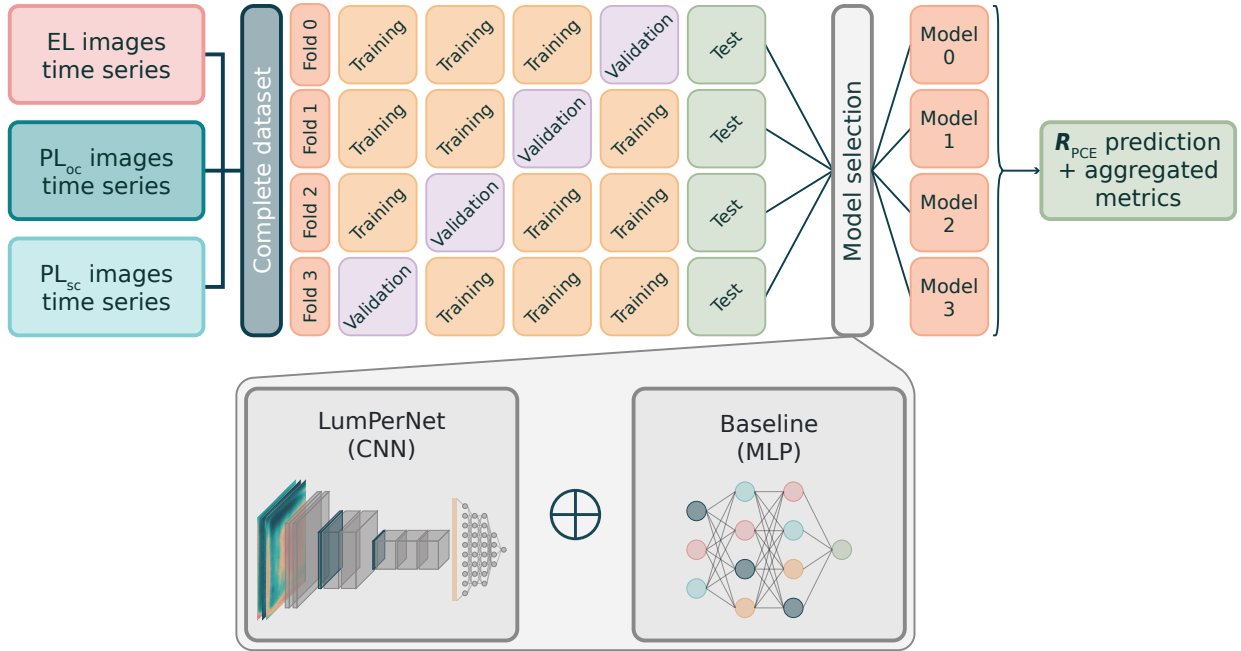


Figure 3: ML framework used in this work. Multimodal luminescence image time series (EL, PL_{oc}, PL_{sc}) constitute the model inputs. Two regressors are benchmarked: LumPerNet, a CNN-based model operating on reference–current image pairs, and a baseline MLP trained on space-averaged intensities. Model selection is performed via four-fold cross-validation within the training–validation subset; for each fold, the best checkpoint is selected on the corresponding validation split and evaluated on the held-out test split. Final predictive performance is reported as the mean across folds, with the fold-to-fold standard deviation reported as an estimate of uncertainty.

and therefore quantifies robustness to training split and optimization history. Figure 4 visualizes predictions on the held-out test set using the ensemble-mean output obtained by averaging the four CV-trained models (one prediction per sample), together with the corresponding absolute error distribution. For completeness, fold-resolved parity plots are reported in the Supplementary Information.

3.2. Baseline comparison: spatial features improve R_{PCE} prediction

To assess whether the predictive signal can be explained solely by global, space-averaged luminescence decay, we benchmark LumPerNet against an intensity-only baseline regressor. The baseline model operates on space-averaged EL, PL_{oc}, and PL_{sc} intensities for each modality and time point, and therefore discards spatial information by construction. LumPerNet, in contrast, learns spatial features from the full multimodal image tensor via convolutional layers.

Both models were trained and evaluated using identical device-level splits and the same two-stage protocol described in Section 2.4, enabling a direct and controlled comparison. On the held-out test set, the intensity-only baseline achieved MAE = 0.064 ± 0.015 , RMSE = 0.082 ± 0.021 , and $R^2 = 0.136 \pm 0.420$ (mean \pm standard deviation across the four CV-trained models). In comparison, as summarized in Figure 5 and Table S1, LumPerNet substantially improves test performance, reducing both MAE and RMSE (-23% and -26% , respectively) while increasing R^2 ($+0.417$ absolute, $\sim 4.1\times$) with lower fold-to-fold variability relative to the intensity-only baseline on the held-out test set under identical splits.

Beyond average performance, the baseline exhibited limited robustness across folds: test R^2 was negative in two of the four runs, indicating that global intensity descriptors alone do not consistently capture the degradation-relevant signal across held-out devices. These results support the use of spatially resolved multimodal imaging and convolutional feature learning for quantitative R_{PCE} estimation, suggesting that localized luminescence patterns provide predictive information beyond mean intensity trends.

We evaluated an additional variant in which models were conditioned on a categorical batch identity via an embedding branch. Here, “batch” denotes the fabrication/testing batch of each device; two batches share the same device

Table 2: Per-fold performance of LumPerNet on the validation and held-out test sets (R_{PCE} prediction). Reported values are computed independently for each fold; the last row summarizes the mean \pm standard deviation across folds. Each fold denotes one cross-validation training run performed on the device-level training-validation subset; the held-out test set contains disjoint devices and is identical across folds.

Fold	Validation			Test (held-out)		
	MAE \downarrow	RMSE \downarrow	R^2 \uparrow	MAE \downarrow	RMSE \downarrow	R^2 \uparrow
0	0.049	0.061	0.467	0.045	0.056	0.624
1	0.073	0.082	0.366	0.050	0.062	0.543
2	0.083	0.105	0.040	0.042	0.057	0.613
3	0.034	0.046	0.754	0.060	0.069	0.432
$\mu \pm \sigma$	0.060 ± 0.019	0.073 ± 0.022	0.407 ± 0.255	0.049 ± 0.006	0.061 ± 0.005	0.553 ± 0.077

architecture but were measured in different campaigns, whereas the third batch corresponds to a different architecture. Batch-conditioning had asymmetric effects across models. For the intensity-only baseline, incorporating batch identity reduced robustness and degraded generalization, increasing fold-to-fold variability and lowering average test performance. For LumPerNet, batch-conditioning did not yield consistent gains and resulted in similar performance to the batch-free setting while increasing model complexity. Accordingly, main-text results are reported without batch information, and the full ablation is provided in the Supplementary Information.

3.3. Ablation on imaging modalities: EL, PL_{oc} , and PL_{sc} are complementary

Having established that spatial information improves prediction beyond global intensity decay, we subsequently quantify in an ablation study whether all three luminescence modalities are needed, or if a reduced input set suffices. To this end, we repeated the full training and evaluation pipeline described in Section 2.4 (device-level held-out test set, four-fold CV on the remaining devices, identical hyperparameters and model capacity) while ablating the input tensor to retain (i) a single modality at a time (EL-only, PL_{oc} -only, or PL_{sc} -only, still including the corresponding aged and reference images, as well as their ratio), and (ii) all coupled two-modality combinations (EL+ PL_{oc} , EL+ PL_{sc} , PL_{oc} + PL_{sc}). The resulting model performance is summarized in Figure 5 and Table S2.

Across all ablations, predictive accuracy degrades relative to the full multimodal LumPerNet model. On the held-out test set, the full model reaches $\text{MAE} = 0.049 \pm 0.007$ and $R^2 = 0.553 \pm 0.077$. In contrast, the single-modality variants yield $\text{MAE} = 0.061 \pm 0.006$ and $R^2 = 0.317 \pm 0.097$ (EL-only), $\text{MAE} = 0.062 \pm 0.005$ and $R^2 = 0.287 \pm 0.102$ (PL_{oc} -only), and $\text{MAE} = 0.063 \pm 0.008$ and $R^2 = 0.215 \pm 0.267$ (PL_{sc} -only), respectively. These results confirm that none of the modalities is individually sufficient to recover the full predictive accuracy.

Coupling modalities partially recovers performance, but the gain depends strongly on *which* modalities are paired. Among two-modality inputs, EL+ PL_{sc} performs best and is closest to the full model, achieving $\text{MAE} = 0.052 \pm 0.002$ and $R^2 = 0.534 \pm 0.034$. Interestingly, PL_{oc} + PL_{sc} is comparably competitive, with $\text{MAE} = 0.051 \pm 0.006$ and $R^2 = 0.461 \pm 0.054$, despite the poor performance of PL_{sc} in isolation. By contrast, EL+ PL_{oc} performs substantially worse ($\text{MAE} = 0.060 \pm 0.005$, $R^2 = 0.245 \pm 0.170$) and exhibits the highest variability across folds, including a near-zero or slightly negative R^2 in one split. This non-trivial behavior indicates that “adding a second modality” does not automatically increase robustness, and that some modality combinations can introduce competing cues that are not consistently transferable across device splits.

A consistent interpretation emerges when considering the device physics of luminescence generation under different conditions. First, both EL and PL_{oc} maps locally probe the relative (and optically modulated) radiative recombination channel at conditions of high quasi Fermi-level splitting, but differ in the mechanism of generation of excited charge carriers. While the carrier generation may be impacted by variations in injection dynamics, the absorption and emission profile and local recombination regions, the similar device condition factors a positive correlation with the local, implied V_{oc} [110]. In contrast, PL_{sc} operates in the carrier extraction regime, where strong quenching of the photoluminescence indicates an effective extraction of charge carriers competing with the radiative (and non-radiative) recombination channels [62, 111]. It therefore has the potential to provide complementary information to the PL_{oc} and EL channels [111, 112]. This is in accordance with our result showing strong model performance of EL+ PL_{sc} and PL_{oc} + PL_{sc} . As expected however, the EL+ PL_{oc} ablation under-performs the other bimodal combinations, indicating the missing complementary information from the PL_{sc} mode.

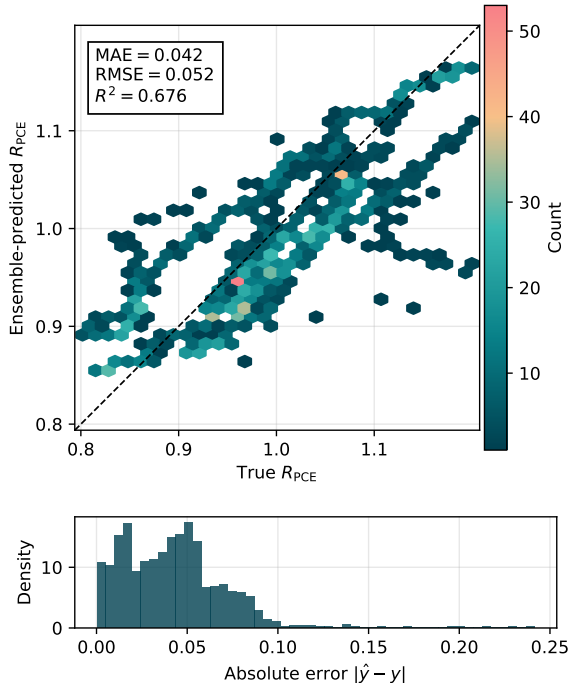


Figure 4: LumPerNet ensemble-mean parity plot and absolute error distribution for R_{PCE} prediction on the held-out test set. This performance is achieved by exploiting spatial patterns rather than only mean intensities (see baseline comparison in Section 3.2). Top: hexbin parity plot comparing measured R_{PCE} to the ensemble-mean prediction \hat{y} , computed by averaging the outputs of the four CV-trained LumPerNet models (one prediction per test sample). Color denotes the number of samples per bin, and the dashed line indicates the ideal $\hat{y} = y$ relationship; inset reports the corresponding ensemble performance metrics. Metrics shown in the inset are computed on the ensemble-mean predictor (mean of the 4 fold-trained models) evaluated on the held-out test set, whereas Table 2 reports mean \pm std across fold-wise test evaluations. The visible banding around the diagonal reflects the longitudinal nature of the test set, with multiple measurements per device that are not statistically independent; device-specific residual structure can therefore emerge as correlated scatter. Bottom: distribution of absolute residuals $|\hat{y} - y|$ over the held-out test samples, summarizing the typical magnitude and spread of prediction errors within the operational range $R_{\text{PCE}} \in [0.8, 1.2]$.

Overall, these ablations support two practical conclusions. First, multimodality is essential for robust generalization: the full model reduces test MAE by about 20% compared to any single-modality alternative and yields a substantially higher R^2 . Second, a carefully chosen bimodal configuration (EL+PL_{sc}, or alternatively PL_{oc}+PL_{sc}) can retain most of the performance of the full model, whereas EL+PL_{oc} is not reliable under the present data splits. Taken together, these results justify the adoption of a multimodal input representation for robust R_{PCE} estimation within the operational window, and motivate reporting bimodal variants only when their cross-fold stability is explicitly verified.

3.4. Qualitative analysis: time-evolving degradation examples

To complement aggregate metrics and parity plots, we qualitatively assess whether point-wise LumPerNet predictions yield temporally reconstructions of degradation trajectories of individual devices. Figure 6 reports three representative trajectories from the held-out test set, covering distinct aging behaviors observed in the dataset. Importantly, LumPerNet does *not* forecast R_{PCE} from earlier data. Instead, each point in the trajectory drawn using LumPerNet is obtained independently from the luminescence images acquired at the corresponding aging time t (together with the device-specific reference images at $t = 0$, i.e., by evaluating the trained regressor on $\mathbf{x}(t)$). Thus, the trajectory is *reconstructed* by repeating the same inference step for all available acquisition times of the device and plotting \hat{R}_{PCE} versus elapsed time. For each device, the measured $R_{\text{PCE}}(t)$, derived from indoor J–V characterization, is

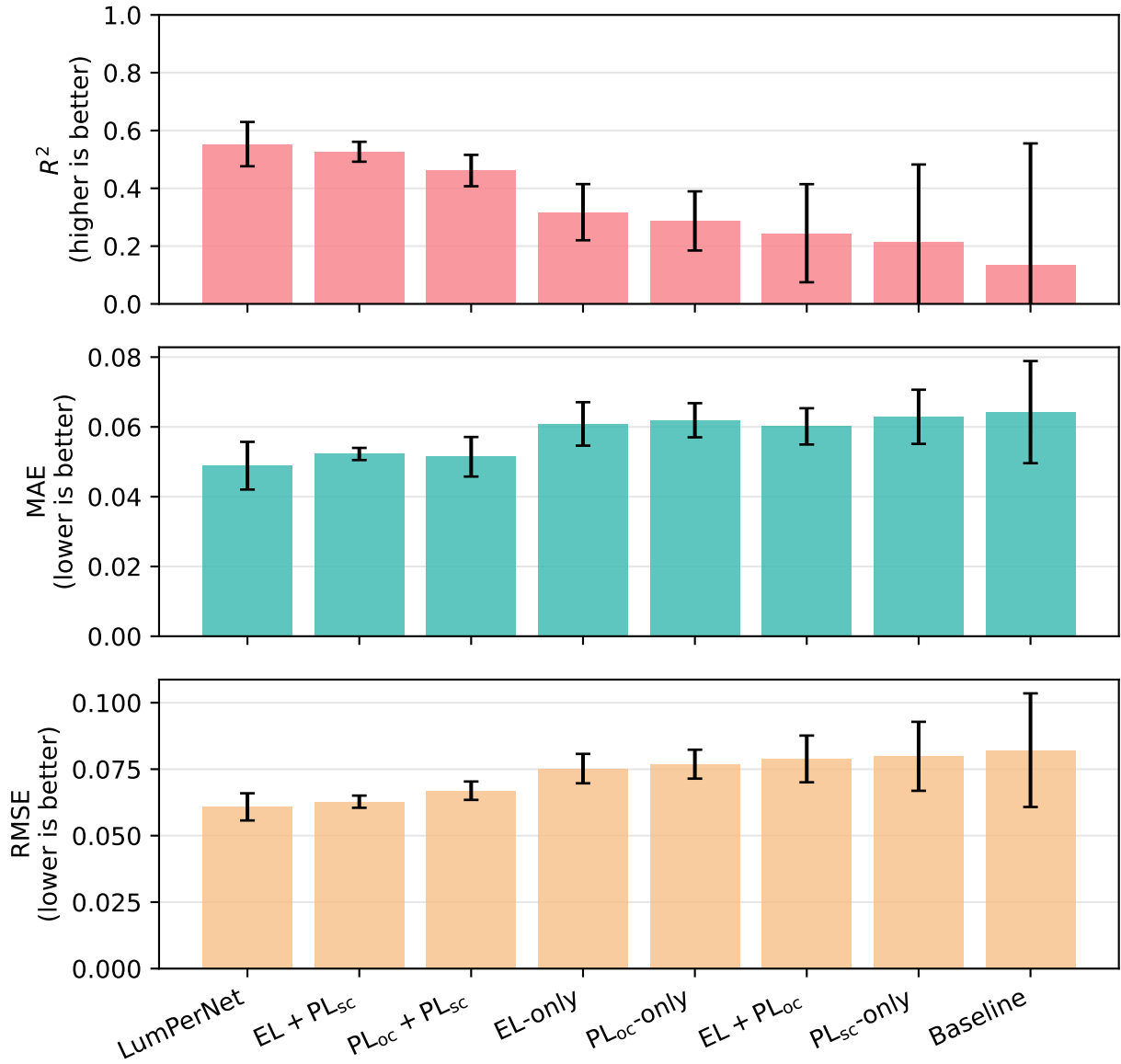


Figure 5: Cross-validated test performance comparison across models under identical device-level splits. Bars report mean \pm standard deviation across the four CV runs on the held-out test set for LumPerNet, single-modality (EL-only, PL_{oc}-only, PL_{sc}-only) and two-modality (EL+PL_{oc}, EL+PL_{sc}, PL_{oc}+PL_{sc}) ablations, and the intensity-only baseline. Higher R^2 and lower MAE/RMSE indicate better performance.

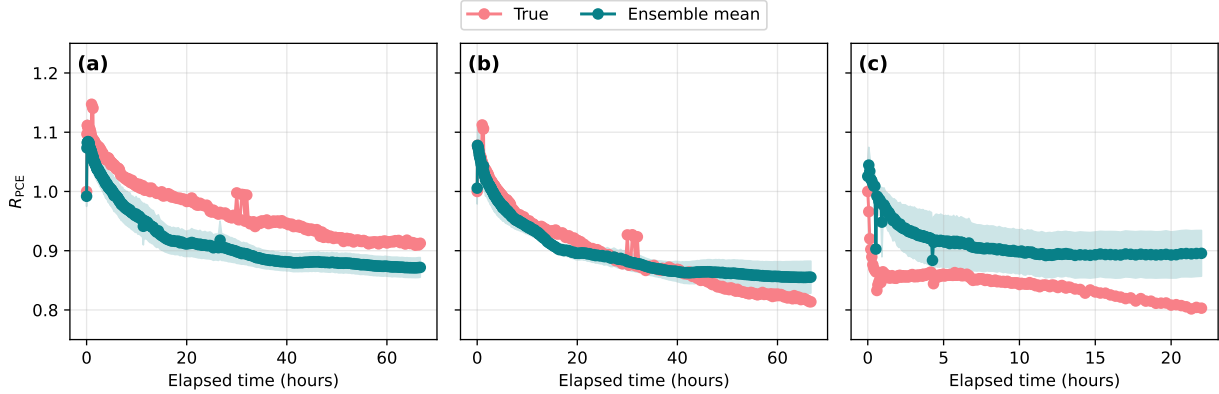


Figure 6: Representative time-evolving $R_{\text{PCE}}(t)$ trajectories reconstructed from LumPerNet predictions on the held-out test set (point-wise inference at acquisition time, not forecasting). Panels (a)–(c) show three devices sharing the same Architecture (A), selected to represent distinct degradation dynamics within our aging dataset: (a) relatively high stability with slow decay, (b) intermediate stability with moderate decay, and (c) relatively low stability with fast decay. Measured $R_{\text{PCE}}(t)$ from indoor J–V characterization (pink) is compared to the LumPerNet ensemble-mean prediction (teal), obtained by averaging predictions from the four cross-validation trained models. At each aging time t , $\hat{R}_{\text{PCE}}(t)$ is obtained by evaluating LumPerNet on the corresponding multimodal images and the $t = 0$ reference state. Shaded regions denote ± 1 standard deviation across models. The horizontal axis reports elapsed time from the start of the aging experiment for each device; luminescence acquisitions are not necessarily performed at uniform intervals, and trajectories may therefore exhibit irregular temporal spacing.

shown alongside the ensemble-mean prediction obtained by averaging the outputs of the four CV-trained LumPerNet models; the shaded band indicates ± 1 standard deviation across models at each acquisition time.

Across these examples, reconstructed trajectories follow the overall evolution of efficiency retention and remain within the operational range of interest. Short-lived excursions in the measured R_{PCE} (e.g., the transient spikes around $t \approx 30$ h in the left and central panels) are not reproduced by the model, consistent with the fact that they may reflect transient electrical effects or measurement artifacts of inconsistent power supply to the incident LEDs rather than persistent changes in luminescence patterns. In addition, some devices exhibit systematic deviations between prediction and measurement, such as an overestimation during extended low- R_{PCE} plateaus (right panel), highlighting challenging regimes that may require larger datasets and, potentially, explicit handling of rapid early transients. Overall, these trajectory-level examples support the quantitative benchmarks by showing that LumPerNet captures the dominant degradation trends while providing a natural measure of inter-model uncertainty through ensemble dispersion.

To complement the trajectory-level visualization in Figure 6, we also quantify how prediction errors are distributed over time across the entire held-out test set. Figure 7 reports the absolute error $|\hat{R}_{\text{PCE}} - R_{\text{PCE}}|$ as a function of elapsed aging time, pooling all test-set samples. This representation makes it possible to identify time windows associated with broader error distributions, and to distinguish isolated high-error events from systematic trends, without relying on a small number of selected devices. Overall, the error distribution remains concentrated at low absolute errors across the majority of the experiment duration, while a broader spread is observed at early times, where rapid transients and reversible effects can induce short-term departures between predicted and measured R_{PCE} . The inset provides a detailed view of the first 15 h, emphasizing that the early-time regime is both the most densely sampled and the most heterogeneous in terms of absolute error.

3.5. Limitations and robustness considerations

While the results above demonstrate the feasibility of regressing PSC state-of-health from multimodal luminescence imaging, the present study remains a proof of concept and has several limitations that contextualize the reported performance. First, the dataset spans 59 devices acquired across three experimental batches. Two batches correspond to the same device architecture measured in different campaigns, whereas the third batch uses a different device architecture (composition and contact stack). This heterogeneity, combined with the limited number of devices relative to the number of sampled time-points, contributes to fold-to-fold variability and motivates cautious interpretation of aggregate metrics.

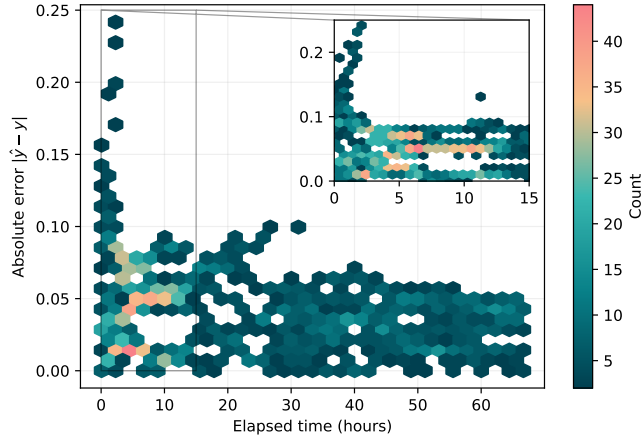


Figure 7: Absolute prediction error versus elapsed time on the held-out test set. Each bin reports the density of test-set samples in the $(t, |\hat{R}_{\text{PCE}} - R_{\text{PCE}}|)$ plane, where t is the elapsed time from the start of aging for each device. The inset highlights the early-time regime (0–15 h), where measurements are most densely sampled and transient effects can lead to increased dispersion in the absolute error.

Second, model predictions are constrained to an operational R_{PCE} window ($R_{\text{PCE}} \in [0.8, 1.2]$) and are trained on samples within this range. As a result, the current framework is not designed to reliably extrapolate to severe end-of-life degradation or to regimes dominated by early transient efficiency gains. Extending the approach to full-lifecycle monitoring will require both broader datasets and explicit handling of out-of-window samples.

Third, the framework was intentionally kept lightweight and was not subjected to extensive hyperparameter optimization or architecture search. Although LumPerNet consistently outperforms an intensity-only baseline under identical splits, further gains may be possible by incorporating richer temporal context (beyond reference–current pairing), improved photometric calibration (e.g., flat-field correction), and additional modalities or physics-informed constraints.

Finally, ablation experiments on batch-conditioning show asymmetric effects across models. For the intensity-only baseline, incorporating batch identity reduced robustness and degraded generalization, suggesting that the categorical batch label can act as a confounding shortcut for global descriptors. For LumPerNet, batch-conditioning did not provide consistent gains and yielded similar performance to the batch-free setting while increasing model complexity. Accordingly, main-text results are reported without batch information, and the full ablation is provided in the Supporting Information.

Overall, these considerations suggest that the primary value of the present work is methodological: it establishes a reproducible, leakage-aware pipeline for coupling time series of luminescence images with electrical labels and demonstrates that spatially resolved multimodal information improves R_{PCE} prediction beyond global intensity trends. A natural extension is a two-stage formulation in which a lightweight classifier first flags samples outside the operational R_{PCE} window, followed by a regressor specialized for the range of interest.

4. Conclusions

This work introduced a deep-learning framework for estimating the R_{PCE} of PSCs from multimodal luminescence imaging acquired during aging. By pairing EL, PL_{oc} , and PL_{sc} images of an aged device state with device-specific reference images, the proposed CNN-based model (LumPerNet) learns spatial degradation signatures and directly regresses the normalized efficiency retention, defined according to Equation 1, within an operational window relevant to stability testing.

Under a leakage-aware evaluation protocol based on device-level held-out testing and cross-validated training, LumPerNet achieves proof-of-concept predictive accuracy in the range $R_{\text{PCE}} \in [0.8, 1.2]$, and qualitatively tracks time-evolving degradation trends across representative devices. Benchmarking against an intensity-only baseline regressor demonstrates the value of spatially resolved feature learning: LumPerNet reduces the held-out test error from $\text{MAE} = 0.064$ to 0.049 (–23.4%) and from $\text{RMSE} = 0.082$ to 0.061 (–25.6%), while improving R^2 from 0.136 to

0.553 (+0.417 absolute, $\sim 4.1\times$). Modality-ablation experiments further clarify the role of multimodality: the full $EL+PL_{oc}+PL_{sc}$ input yields the best generalization, while the single-modality models show a consistent drop in accuracy and cross-fold stability. Importantly, the bimodal results are not monotonic with channel count: $EL+PL_{sc}$ retains most of the full-model performance, and $PL_{oc}+PL_{sc}$ is competitive despite the weaker performance of PL_{sc} in isolation, whereas $EL+PL_{oc}$ is markedly less stable across device splits. Together, these findings support multimodal imaging as a means to capture complementary degradation signatures, and indicate that robustness depends on physically complementary contrast rather than simply adding additional channels. Ablation experiments further highlight that naively incorporating batch identity can act as a confounding shortcut and degrade generalization in the present dataset, motivating the adoption of a batch-identity-free setting as the default for robust performance.

Beyond the specific results reported here, the primary contribution of this work is methodological. The study establishes an end-to-end pipeline linking automated luminescence imaging to indoor electrical labels, with consistent preprocessing, training-time augmentation, and target-distribution balancing, and provides a baseline for future work on scalable, non-invasive degradation monitoring. On the experimental side, future iterations of the acquisition platform will benefit from tighter environmental control (in particular relative-humidity monitoring and control) and improved photometric calibration, to further reduce measurement-induced variability and strengthen dataset consistency. On the modeling side, future efforts will focus on expanding the dataset across device designs and aging conditions and extending the framework toward full-lifecycle monitoring. A promising direction is a two-stage approach that first detects samples outside the operational R_{PCE} range and then applies a dedicated regressor within the region of interest, enabling reliable deployment in accelerated testing and, ultimately, quality-control settings.

More broadly, several complementary directions could be explored toward the same goal of scalable degradation monitoring. These include hybrid formulations that combine learned spatial features with compact physical descriptors or equivalent-circuit parameters, physics-informed or constraint-based learning to enforce monotonicity and operational bounds, and the integration of additional non-invasive channels (for instance temperature or impedance proxies) when available. These outlooks align with the growing adoption of deep learning for image-based monitoring tasks in energy applications [113].

Acknowledgements

S.T. acknowledges the European Union’s Framework Programme for Research and Innovation Horizon Europe (2021–2027) under the Marie Skłodowska-Curie Grant Agreement No. 101107885 “INT-PVK-PRINT”. A.D.C. and S.T. acknowledge the European Union’s Framework Programme for Research and Innovation Horizon Europe (2021–2027) under the Grant Agreement No. 101147311 “LAPERITIVO”. E.C. acknowledges partial support under the National Recovery and Resilience Plan (NRRP), Mission 4 Component 2 Investment 1.3-Call for tender No. 1561 of 11.10.2022 of Ministero dell’Università e della Ricerca (MUR), funded by the European Union NextGenerationEU. We acknowledge AIFAC (project AIFAC_S02_113) for granting access to the LEONARDO supercomputer, owned by the EuroHPC Joint Undertaking, hosted by CINECA (Italy).

CRediT authorship contribution statement

GB: Conceptualization, Data curation, Formal Analysis, Investigation, Methodology, Software, Visualization, Writing – original draft; **ST:** Conceptualization, Data curation, Investigation, Methodology, Writing – review & editing, Supervision; **SA:** Resources, Writing – original draft; **ZA:** Resources, Writing – original draft; **CO:** Resources, Writing – original draft; **MDA:** Resources, Writing – original draft; **EM:** Resources, Writing – original draft; **PA:** Conceptualization, Funding acquisition, Project administration, Supervision, Writing – review & editing; **EC:** Conceptualization, Funding acquisition, Project administration, Resources, Supervision, Writing – review & editing; **ADC:** Conceptualization, Funding acquisition, Project administration, Resources, Supervision, Writing – review & editing.

All authors read and approved the final manuscript.

Additional information

Supporting Information is available with this article and includes measured LED emission spectra, photographs of the custom-built acquisition setup, detailed model architectures and hyperparameters, and extended results (complete tables, per-fold parity plots and ablation studies).

Portions of the wording in this work were refined with the assistance of ChatGPT, an AI language model by OpenAI, in accordance with the CC-BY 4.0 license; the underlying content was developed by the authors.

Code availability

The entire workflow is managed through Python scripts provided and maintained in the GitHub repository (<https://github.com/giuliobarl/LumPerNet>).

Data availability

The processed dataset used to train the models presented in this article are publicly available in the Zenodo repository (<https://doi.org/10.5281/zenodo.18700767>).

Competing interests

The authors declare no competing financial interest.

References

- [1] M. A. Green, E. D. Dunlop, M. Yoshita, N. Kopidakis, K. Bothe, G. Siefert et al., Solar Cell Efficiency Tables (Version 66), *Progress in Photovoltaics: Research and Applications* 33 (7) (2025) 795–810. doi:10.1002/pip.3919.
- [2] A. Kojima, K. Teshima, Y. Shirai, T. Miyasaka, Organometal Halide Perovskites as Visible-Light Sensitizers for Photovoltaic Cells, *J. Am. Chem. Soc.* 131 (17) (2009) 6050–6051. doi:10.1021/ja809598r.
- [3] M. A. Green, A. Ho-Baillie, H. J. Snaith, The emergence of perovskite solar cells, *Nature Photon* 8 (7) (2014) 506–514. doi:10.1038/nphoton.2014.134.
- [4] H. S. Jung, N.-G. Park, Perovskite Solar Cells: From Materials to Devices, *Small* 11 (1) (2015) 10–25. doi:10.1002/sml.201402767.
- [5] J. Y. Kim, J.-W. Lee, H. S. Jung, H. Shin, N.-G. Park, High-Efficiency Perovskite Solar Cells, *Chem. Rev.* 120 (15) (2020) 7867–7918. doi:10.1021/acs.chemrev.0c00107.
- [6] J.-P. Correa-Baena, M. Saliba, T. Buonassisi, M. Grätzel, A. Abate, W. Tress et al., Promises and challenges of perovskite solar cells, *Science* 358 (6364) (2017) 739–744. doi:10.1126/science.aam6323.
- [7] Z. Xiong, Q. Zhang, K. Cai, H. Zhou, Q. Song, Z. Han et al., Homogenized chlorine distribution for >27% power conversion efficiency in perovskite solar cells, *Science* 390 (6773) (2025) 638–642. doi:10.1126/science.adw8780.
- [8] LONGi sets new world record with 27.30% for heterojunction back contact cells and renames next generation silicon tera wafer to TaiRay Wafer (2024).
URL <https://www.longi.com/eu/news/2730-hbc-world-record/>
- [9] 34.85%! LONGi Breaks World Record for Crystalline Silicon-Perovskite Tandem Solar Cell Efficiency Again (2025).
URL <https://www.longi.com/en/news/silicon-perovskite-tandem-solar-cells-new-world-efficiency/>

- [10] R. Lin, H. Gao, J. Lou, J. Xu, M. Yin, P. Wu et al., All-perovskite tandem solar cells with dipolar passivation, *Nature* 648 (8094) (2025) 600–606. doi:10.1038/s41586-025-09773-7.
- [11] M. V. Khenkin, E. A. Katz, A. Abate, G. Bardizza, J. J. Berry, C. Brabec et al., Consensus statement for stability assessment and reporting for perovskite photovoltaics based on ISOS procedures, *Nat Energy* 5 (1) (2020) 35–49. doi:10.1038/s41560-019-0529-5.
- [12] R. Wang, M. Mujahid, Y. Duan, Z.-K. Wang, J. Xue, Y. Yang, A Review of Perovskites Solar Cell Stability, *Advanced Functional Materials* 29 (47) (2019) 1808843. doi:10.1002/adfm.201808843.
- [13] P. T. Mokabane, V. T. Lukong, T.-C. Jen, A review of the effect of stability issues and wide-bandgap in the application of perovskite solar cells, *Mater Renew Sustain Energy* 14 (2) (2025) 34. doi:10.1007/s40243-025-00307-9.
- [14] N. Yaghoobi Nia, M. Zendejdel, B. Paci, J. Xu, M. Di Giovannantonio, A. Generosi et al., Co-crystal engineering of a two-dimensional perovskite phase for perovskite solar modules with improved efficiency and stability, *Nat Energy* 11 (1) (2026) 135–149. doi:10.1038/s41560-025-01903-9.
- [15] M. A. Fazal, S. Rubaiee, Progress of PV cell technology: Feasibility of building materials, cost, performance, and stability, *Solar Energy* 258 (2023) 203–219. doi:10.1016/j.solener.2023.04.066.
- [16] H. Cui, G. Heath, T. Remo, D. Ravikumar, T. Silverman, M. Deceglie et al., Technoeconomic analysis of high-value, crystalline silicon photovoltaic module recycling processes, *Solar Energy Materials and Solar Cells* 238 (2022) 111592. doi:10.1016/j.solmat.2022.111592.
- [17] Y. Chen, D. Chen, P. P. Altermatt, S. Zhang, L. Wang, X. Zhang et al., Technology evolution of the photovoltaic industry: Learning from history and recent progress, *Progress in Photovoltaics: Research and Applications* 31 (12) (2023) 1194–1204. doi:10.1002/pip.3626.
- [18] J. Bian, L. Li, L. Chen, W. Zhu, T. Zhang, Y. Liu et al., Unraveling of the reversible light soaking mechanisms in intrinsic halide perovskite film, *Journal of Power Sources* 653 (2025) 237704. doi:10.1016/j.jpowsour.2025.237704.
- [19] L. Lin, L. Yang, G. Du, X. Li, Y.-n. Li, J. Deng et al., Light Soaking Effects in Perovskite Solar Cells: Mechanism, Impacts, and Elimination, *ACS Appl. Energy Mater.* 6 (20) (2023) 10303–10318. doi:10.1021/acsaem.2c04120.
- [20] Z. Ahmad, M. A. Najeeb, R. A. Shakoor, A. Alashraf, S. A. Al-Muhtaseb, A. Soliman et al., Instability in CH₃NH₃PbI₃ perovskite solar cells due to elemental migration and chemical composition changes, *Sci Rep* 7 (1) (2017) 15406. doi:10.1038/s41598-017-15841-4.
- [21] N. Kalasariya, P. F. Sowmeeh, F. Pena-Camargo, F. Vanin, T. Lukas, Y. Dong et al., How Halide Segregation Governs the Ion Density Evolution and Ionic Performance Losses: From Degradation to Recovery, *Advanced Energy Materials* (2026) e03866doi:10.1002/aenm.202503866.
- [22] J. T. DuBose, P. V. Kamat, Hole Trapping in Halide Perovskites Induces Phase Segregation, *Acc. Mater. Res.* 3 (7) (2022) 761–771. doi:10.1021/accountsmr.2c00076.
- [23] Y. Guo, C. Zhang, L. Wang, X. Yin, B. Sun, C. Wei et al., Unveiling the impact of photoinduced halide segregation on performance degradation in wide-bandgap perovskite solar cells, *Energy & Environmental Science* 18 (5) (2025) 2308–2317. doi:10.1039/D4EE05604C.
- [24] H. Zhu, S. Teale, M. N. Lintangpradipto, S. Mahesh, B. Chen, M. D. McGehee et al., Long-term operating stability in perovskite photovoltaics, *Nat Rev Mater* 8 (9) (2023) 569–586. doi:10.1038/s41578-023-00582-w.

- [25] T. Ahmed Chowdhury, M. A. B. Zafar, M. S.-U. Islam, M. Shahinuzzaman, M. Aminul Islam, M. Uddin Khadaker, Stability of perovskite solar cells: issues and prospects, *RSC Advances* 13 (3) (2023) 1787–1810. doi:10.1039/D2RA05903G.
- [26] H.-S. Kim, J.-Y. Seo, N.-G. Park, Material and Device Stability in Perovskite Solar Cells, *ChemSusChem* 9 (18) (2016) 2528–2540. doi:10.1002/cssc.201600915.
- [27] T. J. Silverman, M. G. Deceglie, I. Repins, M. Owen-Bellini, J. J. Berry, J. S. Stein et al., Durability research is pivotal for perovskite photovoltaics, *Nat Energy* 10 (8) (2025) 934–940. doi:10.1038/s41560-025-01786-w.
- [28] Q. Jiang, R. Tirawat, R. A. Kerner, E. A. Gauling, Y. Xian, X. Wang et al., Towards linking lab and field lifetimes of perovskite solar cells, *Nature* 623 (7986) (2023) 313–318. doi:10.1038/s41586-023-06610-7.
- [29] M. Jošt, B. Lipovšek, B. Glažar, A. Al-Ashouri, K. Brecl, G. Matič et al., Perovskite Solar Cells go Outdoors: Field Testing and Temperature Effects on Energy Yield, *Advanced Energy Materials* 10 (25) (2020) 2000454. doi:10.1002/aenm.202000454.
- [30] G. M. Meheretu, A. K. Worku, M. T. Yihunie, R. K. Koech, G. A. Wubetu, The recent advancement of outdoor performance of perovskite photovoltaic cells technology, *Heliyon* 10 (17) (Sep. 2024). doi:10.1016/j.heliyon.2024.e36710.
- [31] T. J. Jacobsson, A. Hultqvist, A. García-Fernández, A. Anand, A. Al-Ashouri, A. Hagfeldt et al., An open-access database and analysis tool for perovskite solar cells based on the FAIR data principles, *Nat Energy* 7 (1) (2022) 107–115. doi:10.1038/s41560-021-00941-3.
- [32] M. Nur-E-Alam, M. S. Islam, T. Abedin, M. A. Islam, B. K. Yap, T. S. Kiong et al., Current scenario and future trends on stability issues of perovskite solar cells: A mini review, *Current Opinion in Colloid & Interface Science* 76 (2025) 101895. doi:10.1016/j.cocis.2025.101895.
- [33] R. Azmi, E. Ugur, A. Seitkhan, F. Aljamaan, A. S. Subbiah, J. Liu et al., Damp heat-stable perovskite solar cells with tailored-dimensionality 2D/3D heterojunctions, *Science* 376 (6588) (2022) 73–77. doi:10.1126/science.abm5784.
- [34] A. Mavlonov, Y. Hishikawa, Y. Kawano, T. Negami, A. Hayakawa, S. Tsujimura et al., Thermal stability test on flexible perovskite solar cell modules to estimate activation energy of degradation on temperature, *Solar Energy Materials and Solar Cells* 277 (2024) 113148. doi:10.1016/j.solmat.2024.113148.
- [35] M. N. Lintangpradipto, H. Zhu, B. Shao, W. J. Mir, L. Gutiérrez-Arzaluz, B. Turedi et al., Single-Crystal Methylammonium-Free Perovskite Solar Cells with Efficiencies Exceeding 24% and High Thermal Stability, *ACS Energy Lett.* 8 (11) (2023) 4915–4922. doi:10.1021/acsenerylett.3c01935.
- [36] M. O. Reese, S. A. Gevorgyan, M. Jørgensen, E. Bundgaard, S. R. Kurtz, D. S. Ginley et al., Consensus stability testing protocols for organic photovoltaic materials and devices, *Solar Energy Materials and Solar Cells* 95 (5) (2011) 1253–1267. doi:10.1016/j.solmat.2011.01.036.
- [37] M. V. Khenkin, A. K. M, I. Visoly-Fisher, Y. Galagan, F. D. Giacomo, B. Ramesh Patil et al., Reconsidering figures of merit for performance and stability of perovskite photovoltaics, *Energy & Environmental Science* 11 (4) (2018) 739–743. doi:10.1039/C7EE02956J.
- [38] N. Aristidou, I. Sanchez-Molina, T. Chotchuangchutchaval, M. Brown, L. Martinez, T. Rath et al., The Role of Oxygen in the Degradation of Methylammonium Lead Trihalide Perovskite Photoactive Layers, *Angewandte Chemie International Edition* 54 (28) (2015) 8208–8212. doi:10.1002/anie.201503153.
- [39] J. Thiesbrummel, S. Shah, E. Gutierrez-Partida, F. Zu, F. Peña-Camargo, S. Zeiske et al., Ion-induced field screening as a dominant factor in perovskite solar cell operational stability, *Nat Energy* 9 (6) (2024) 664–676. doi:10.1038/s41560-024-01487-w.

- [40] J. A. Kress, C. Quarti, Q. An, S. Bitton, N. Tessler, D. Beljonne et al., Persistent Ion Accumulation at Interfaces Improves the Performance of Perovskite Solar Cells, *ACS Energy Lett.* 7 (10) (2022) 3302–3310. doi:10.1021/acsenerylett.2c01636.
- [41] S. Moghadamzadeh, I. M. Hossain, M. Jakoby, B. A. Nejang, D. Rueda-Delgado, J. A. Schwenzler et al., Spontaneous enhancement of the stable power conversion efficiency in perovskite solar cells, *Journal of Materials Chemistry A* 8 (2) (2020) 670–682. doi:10.1039/C9TA09584E.
- [42] S. Shao, M. Abdu-Aguye, L. Qiu, L.-H. Lai, J. Liu, S. Adjokatse et al., Elimination of the light soaking effect and performance enhancement in perovskite solar cells using a fullerene derivative, *Energy & Environmental Science* 9 (7) (2016) 2444–2452. doi:10.1039/C6EE01337F.
- [43] B. P. Finkenauer, Akriti, K. Ma, L. Dou, Degradation and Self-Healing in Perovskite Solar Cells, *ACS Appl. Mater. Interfaces* 14 (21) (2022) 24073–24088. doi:10.1021/acsaem.1c01925.
- [44] M. Prete, M. V. Khenkin, D. Glowienka, B. R. Patil, J. S. Lissau, I. Dogan et al., Bias-Dependent Dynamics of Degradation and Recovery in Perovskite Solar Cells, *ACS Appl. Energy Mater.* 4 (7) (2021) 6562–6573. doi:10.1021/acsaem.1c00588.
- [45] Y. Song, Z. Liu, X. Cai, H. Ge, X. Liu, X. Wang et al., Efficient and Moisture Resistant Wide-Bandgap Perovskite Solar Cells with Phosphinate-Based Iodine Defect Passivation, *Advanced Energy Materials* 15 (30) (2025) 2500650. doi:10.1002/aenm.202500650.
- [46] T. Chen, J. Xie, P. Gao, Ultraviolet Photocatalytic Degradation of Perovskite Solar Cells: Progress, Challenges, and Strategies, *Advanced Energy and Sustainability Research* 3 (6) (2022) 2100218. doi:10.1002/aesr.202100218.
- [47] S.-W. Lee, S. Kim, S. Bae, K. Cho, T. Chung, L. E. Mundt et al., UV Degradation and Recovery of Perovskite Solar Cells, *Sci Rep* 6 (1) (2016) 38150. doi:10.1038/srep38150.
- [48] A. Farooq, I. M. Hossain, S. Moghadamzadeh, J. A. Schwenzler, T. Abzieher, B. S. Richards et al., Spectral Dependence of Degradation under Ultraviolet Light in Perovskite Solar Cells, *ACS Appl. Mater. Interfaces* 10 (26) (2018) 21985–21990. doi:10.1021/acsaem.8b03024.
- [49] J. Li, Q. Dong, N. Li, L. Wang, Direct Evidence of Ion Diffusion for the Silver-Electrode-Induced Thermal Degradation of Inverted Perovskite Solar Cells, *Advanced Energy Materials* 7 (14) (2017) 1602922. doi:10.1002/aenm.201602922.
- [50] M. Qi, L. Jin, H. Yao, Z. Xu, T. Cheng, Q. Chen et al., Recent progress on electrical failure and stability of perovskite solar cells under reverse bias, *Acta Physico-Chimica Sinica* 41 (8) (2025) 100088. doi:10.1016/j.actphy.2025.100088.
- [51] S. Bae, S. Kim, S.-W. Lee, K. J. Cho, S. Park, S. Lee et al., Electric-Field-Induced Degradation of Methylammonium Lead Iodide Perovskite Solar Cells, *J. Phys. Chem. Lett.* 7 (16) (2016) 3091–3096. doi:10.1021/acscjpclett.6b01176.
- [52] P. Jowett, Oxford PV starts commercial distribution of perovskite solar modules (Sep. 2024). URL <https://www.pv-magazine.com/2024/09/05/oxford-pv-starts-commercial-distribution-of-perovskite-solar-modules/>
- [53] R. Kennedy, Plenitude tests perovskite-silicon tandem solar modules in utility-scale installation pilot (Nov. 2025). URL <https://www.pv-magazine.com/2025/11/26/plenitude-tests-perovskite-silicon-tandem-solar-modules-in-utility-scale-installation-pilot/>

- [54] V. Shaw, Chinese PV Industry Brief: PowerChina signs 1.05 GW Terra solar deal (Dec. 2024).
URL <https://www.pv-magazine.com/2024/12/03/chinese-pv-industry-brief-powerchina-signs-1-05-gw-terra-solar-deal/>
- [55] V. E. Puranik, R. Kumar, R. Gupta, Progress in module level quantitative electroluminescence imaging of crystalline silicon PV module: A review, *Solar Energy* 264 (2023) 111994. doi:10.1016/j.solener.2023.111994.
- [56] Z. Wang, P. Zheng, B. Bahadir Kocer, M. Kovac, Drone-Based Solar Cell Inspection With Autonomous Deep Learning, in: *Infrastructure Robotics*, John Wiley & Sons, Ltd, 2024, pp. 337–365. doi:10.1002/9781394162871.ch16.
- [57] B. Doll, J. Hepp, M. Hoffmann, R. Schüler, C. Buerhop-Lutz, I. M. Peters et al., Photoluminescence for Defect Detection on Full-Sized Photovoltaic Modules, *IEEE Journal of Photovoltaics* 11 (6) (2021) 1419–1429. doi:10.1109/JPHOTOV.2021.3099739.
- [58] B. Chen, J. Peng, H. Shen, T. Duong, D. Walter, S. Johnston et al., Imaging Spatial Variations of Optical Bandgaps in Perovskite Solar Cells, *Advanced Energy Materials* 9 (7) (2019) 1802790. doi:10.1002/aenm.201802790.
- [59] A. M. Soufiani, M. J. Y. Tayebjee, S. Meyer, A. Ho-Baillie, J. Sung Yun, R. W. MacQueen et al., Electro- and photoluminescence imaging as fast screening technique of the layer uniformity and device degradation in planar perovskite solar cells, *J. Appl. Phys.* 120 (3) (2016) 035702. doi:10.1063/1.4956436.
- [60] T. Mariam, Z. S. Almutawah, A. B. Phillips, S. Fu, J. Chung, Y. Li et al., Environmentally Controlled Electroluminescence/Photoluminescence Imaging System with Current Density-Voltage Capabilities for Quantitative Degradation Analysis of Perovskite Thin Film Solar Cells, in: *2023 IEEE 50th Photovoltaic Specialists Conference (PVSC)*, 2023, pp. 1–6. doi:10.1109/PVSC48320.2023.10359933.
- [61] J. W. Schall, A. Glaws, N. Y. Doumon, T. J. Silverman, M. Owen-Bellini, K. Terwilliger et al., Accelerated Stress Testing of Perovskite Photovoltaic Modules: Differentiating Degradation Modes with Electroluminescence Imaging, *Solar RRL* 7 (14) (2023) 2300229. doi:10.1002/solr.202300229.
- [62] V. Campanari, F. Martelli, A. Agresti, S. Pescetelli, N. Y. Nia, F. Di Giacomo et al., Reevaluation of Photoluminescence Intensity as an Indicator of Efficiency in Perovskite Solar Cells, *Solar RRL* 6 (8) (2022) 2200049. doi:10.1002/solr.202200049.
- [63] X. Geng, Y. Liu, X. Zou, E. M. J. Johansson, J. Sá, Can photoluminescence quenching be a predictor for perovskite solar cell efficiencies?, *Physical Chemistry Chemical Physics* 25 (34) (2023) 22607–22613. doi:10.1039/D3CP02190D.
- [64] S. Kim, J. H. Jang, Z. Wu, M. J. Lee, H. Y. Woo, I. Hwang, Interfacial Defects Change the Correlation between Photoluminescence, Ideality Factor, and Open-Circuit Voltage in Perovskite Solar Cells, *Small* 17 (33) (2021) 2101839. doi:10.1002/smll.202101839.
- [65] L. Krückemeier, B. Krogmeier, Z. Liu, U. Rau, T. Kirchartz, Understanding Transient Photoluminescence in Halide Perovskite Layer Stacks and Solar Cells, *Advanced Energy Materials* 11 (19) (2021) 2003489. doi:10.1002/aenm.202003489.
- [66] R. Dileep K, S. Mandati, E. Ramasamy, S. Mallick, T. N. Rao, G. Veerappan, Rapid assessment of photovoltaic activity of perovskite solar cells by photoluminescence spectroscopy, *Materials Letters* 299 (2021) 130056. doi:10.1016/j.matlet.2021.130056.
- [67] B. Hacene, F. Laufer, S. Ternes, A. Farag, R. Pappenberger, P. Fassl et al., Intensity Dependent Photoluminescence Imaging for In-Line Quality Control of Perovskite Thin Film Processing, *Advanced Materials Technologies* 9 (11) (2024) 2301279. doi:10.1002/admt.202301279.

- [68] P. Basumatary, J. Kumari, P. Agarwal, Probing the defects states in MAPbI₃ perovskite thin films through photoluminescence and photoluminescence excitation spectroscopy studies, *Optik* 266 (2022) 169586. doi:10.1016/j.ijleo.2022.169586.
- [69] J. Chen, C. Zhang, X. Liu, L. Peng, J. Lin, X. Chen, Carrier dynamic process in all-inorganic halide perovskites explored by photoluminescence spectra, *Photon. Res., PRJ* 9 (2) (2021) 151–170. doi:10.1364/PRJ.410290.
- [70] H. Wu, J. Zhang, Y. Zhang, F. Cao, Z. Qiu, L. Zhang et al., Anomalous Electroluminescence Characteristics of Perovskite Modules, *ACS Appl. Mater. Interfaces* 16 (32) (2024) 41986–41995. doi:10.1021/acscami.4c03397.
- [71] M. A. Torre Cachafeiro, E. L. Comi, S. Parayil Shaji, S. Narbey, S. Jenatsch, E. Knapp et al., Ion Migration in Mesoscopic Perovskite Solar Cells: Effects on Electroluminescence, Open Circuit Voltage, and Photovoltaic Quantum Efficiency, *Advanced Energy Materials* 15 (5) (2025) 2403850. doi:10.1002/aenm.202403850.
- [72] M. Gao, Y. Xie, P. Song, J. Qian, X. Sun, J. Liu, A Definition Rule for Defect Classification and Grading of Solar Cells Photoluminescence Feature Images and Estimation of CNN-Based Automatic Defect Detection Method, *Crystals* 13 (5) (2023) 819. doi:10.3390/cryst13050819.
- [73] B. Louis, S. Seth, Q. An, R. Ji, Y. Vaynzof, J. Hofkens et al., In Operando Locally-Resolved Photophysics in Perovskite Solar Cells by Correlation Clustering Imaging, *Advanced Materials* 37 (7) (2025) 2413126. doi:10.1002/adma.202413126.
- [74] N. Taherimakhsoosi, B. P. MacLeod, F. G. L. Parlane, T. D. Morrissey, E. P. Booker, K. E. Dettelbach et al., Quantifying defects in thin films using machine vision, *npj Comput Mater* 6 (1) (2020) 111. doi:10.1038/s41524-020-00380-w.
- [75] S. Ternes, F. Laufer, P. Scharfer, W. Schabel, B. S. Richards, I. A. Howard et al., Correlative In Situ Multichannel Imaging for Large-Area Monitoring of Morphology Formation in Solution-Processed Perovskite Layers, *Solar RRL* 6 (3) (2022) 2100353. doi:10.1002/solr.202100353.
- [76] F. Laufer, S. Ziegler, F. Schackmar, E. A. Moreno Viteri, M. Götz, C. Debus et al., Process Insights into Perovskite Thin-Film Photovoltaics from Machine Learning with In Situ Luminescence Data, *Solar RRL* 7 (7) (2023) 2201114. doi:10.1002/solr.202201114.
- [77] F. Laufer, M. Götz, U. W. Paetzold, Deep learning for augmented process monitoring of scalable perovskite thin-film fabrication, *Energy & Environmental Science* 18 (4) (2025) 1767–1782. doi:10.1039/D4EE03445G.
- [78] J. Kumar, B. Nath, T. Bhattacharjee, P. C. Ramamurthy, Machine learning aided optoelectric characterization modelling and prediction of the IV parameters of perovskite solar cells with > 90% accuracy, *Sci Rep* 15 (1) (2025) 30660. doi:10.1038/s41598-025-93004-6.
- [79] R. Zhang, B. Motes, S. Tan, Y. Lu, M.-C. Shih, Y. Hao et al., Machine Learning Prediction of Organic–Inorganic Halide Perovskite Solar Cell Performance from Optical Properties, *ACS Energy Lett.* 10 (4) (2025) 1714–1724. doi:10.1021/acsenerylett.4c03592.
- [80] A. Glaws, J. W. Schall, A. Ballen, A. E. Louks, K. O. Davis, A. F. Palmstrom et al., Explainable artificial intelligence relates perovskite luminescence images to current-voltage metrics, *Energy and AI* 22 (2025) 100640. doi:10.1016/j.egyai.2025.100640.
- [81] Ç. Odabaşı, R. Yıldırım, Machine learning analysis on stability of perovskite solar cells, *Solar Energy Materials and Solar Cells* 205 (2020) 110284. doi:10.1016/j.solmat.2019.110284.
- [82] Y. Hu, X. Hu, L. Zhang, T. Zheng, J. You, B. Jia et al., Machine-Learning Modeling for Ultra-Stable High-Efficiency Perovskite Solar Cells, *Advanced Energy Materials* 12 (41) (2022) 2201463. doi:10.1002/aenm.202201463.

- [83] S. Zhao, S. Zhou, Z. Guo, H. Luo, Z. Jiang, N. Lin et al., Machine Learning-Assisted Analysis of Perovskite Solar Cell Long-Term Stability under Multiple Environmental Factors, *ACS Sustainable Chem. Eng.* 13 (19) (2025) 7155–7165. doi:10.1021/acssuschemeng.5c01361.
- [84] M. Mammeri, H. Bencherif, L. Dehimi, A. Hajri, P. Sasikumar, A. Syed et al., Stability forecasting of perovskite solar cells utilizing various machine learning and deep learning techniques, *J Opt* 54 (3) (2025) 930–938. doi:10.1007/s12596-024-01819-9.
- [85] M. Srivastava, A. R. Hering, Y. An, J.-P. Correa-Baena, M. S. Leite, Machine Learning Enables Prediction of Halide Perovskites' Optical Behavior with >90% Accuracy, *ACS Energy Lett.* 8 (4) (2023) 1716–1722. doi:10.1021/acsenenergylett.2c02555.
- [86] K. Ji, W. Lin, Y. Sun, L.-S. Cui, J. Shamsi, Y.-H. Chiang et al., Self-supervised deep learning for tracking degradation of perovskite light-emitting diodes with multispectral imaging, *Nat Mach Intell* 5 (11) (2023) 1225–1235. doi:10.1038/s42256-023-00736-z.
- [87] X. Zhao, T. Liu, Q. C. Burlingame, T. Liu, R. Holley, G. Cheng et al., Accelerated aging of all-inorganic, interface-stabilized perovskite solar cells, *Science* 377 (6603) (2022) 307–310. doi:10.1126/science.abn5679.
- [88] A. Pandey, A. Bag, Progress and perspectives on accelerated degradation modeling of perovskite solar cells, *Renewable and Sustainable Energy Reviews* 225 (2026) 116173. doi:10.1016/j.rser.2025.116173.
- [89] T. Ye, Y.-Y. Sun, M. Kocherga, A. Nesmelov, T. A. Schmedake, Y. Zhang, Degradation Kinetics of Organic–Inorganic Hybrid Materials from Micro-Raman Spectroscopy and Density-Functional Theory: The Case of β -ZnTe(en)_{0.5}, *Small* 19 (42) (2023) 2302935. doi:10.1002/smll.202302935.
- [90] R. Tirawat, A. E. Louks, M. Yang, S. N. Habisreutinger, J. v. d. Lagemaat, S. Uličná et al., Measuring metal halide perovskite single cell degradation consistent with module-based conditions, *Sustainable Energy Fuels* 8 (3) (2024) 546–553. doi:10.1039/D3SE01268A.
- [91] E. v. Hauff, D. Klotz, Impedance spectroscopy for perovskite solar cells: characterisation, analysis, and diagnosis, *Journal of Materials Chemistry C* 10 (2) (2022) 742–761. doi:10.1039/D1TC04727B.
- [92] M. He, Y. Ma, S. Wu, H. Tan, D. Wenlong, L. Liu et al., Amorphous grain boundary engineering for scalable flexible perovskite photovoltaics with improved stability, *Nat Energy* 11 (2) (2026) 262–273. doi:10.1038/s41560-025-01932-4.
- [93] A. Tiihonen, K. Miettunen, J. Halme, S. Lepikko, A. Poskela, P. D. Lund, Critical analysis on the quality of stability studies of perovskite and dye solar cells, *Energy & Environmental Science* 11 (4) (2018) 730–738. doi:10.1039/C7EE02670F.
- [94] E. Magliano, F. Di Giacomo, H. R. Sathy, S. M. Pourmotlagh, G. Giliberti, D. Becerril Rodriguez et al., Solution-Processed Metal-Oxide Nanoparticles to Prevent The Sputtering Damage in Perovskite/Silicon Tandem Solar Cells, *ACS Appl. Mater. Interfaces* 17 (11) (2025) 17599–17610. doi:10.1021/acsam.5c00090.
- [95] C. R. Harris, K. J. Millman, S. J. van der Walt, R. Gommers, P. Virtanen, D. Cournapeau et al., Array programming with NumPy, *Nature* 585 (7825) (2020) 357–362. doi:10.1038/s41586-020-2649-2.
- [96] W. McKinney, Data Structures for Statistical Computing in Python, *SciPy 2010* (May 2010). doi:10.25080/Majora-92bf1922-00a.
- [97] P. Virtanen, R. Gommers, T. E. Oliphant, M. Haberland, T. Reddy, D. Cournapeau et al., SciPy 1.0: fundamental algorithms for scientific computing in Python, *Nat Methods* 17 (3) (2020) 261–272. doi:10.1038/s41592-019-0686-2.

- [98] J. D. Hunter, Matplotlib: A 2D Graphics Environment, *Computing in Science & Engineering* 9 (3) (2007) 90–95. doi:10.1109/MCSE.2007.55.
- [99] C. Gohlke, *cgohlke/tiff*file: v2025.10.16 (Oct. 2025). doi:10.5281/ZENODO.6795860. URL <https://zenodo.org/doi/10.5281/zenodo.6795860>
- [100] J. C. Russ, *The Image Processing Handbook*, 6th Edition, CRC Press, Boca Raton, 2016. doi:10.1201/b10720.
- [101] Z. Zhang, H. Wang, T. J. Jacobsson, J. Luo, Big data driven perovskite solar cell stability analysis, *Nat Commun* 13 (1) (2022) 7639. doi:10.1038/s41467-022-35400-4.
- [102] C. L. Watts, L. Aspitarte, Y.-H. Lin, W. Li, R. Elzein, R. Addou et al., Light soaking in metal halide perovskites studied via steady-state microwave conductivity, *Commun Phys* 3 (1) (2020) 73. doi:10.1038/s42005-020-0350-2.
- [103] C. Zhao, B. Chen, X. Qiao, L. Luan, K. Lu, B. Hu, Revealing Underlying Processes Involved in Light Soaking Effects and Hysteresis Phenomena in Perovskite Solar Cells, *Advanced Energy Materials* 5 (14) (2015) 1500279. doi:10.1002/aenm.201500279.
- [104] W. Tress, M. Yavari, K. Domanski, P. Yadav, B. Niesen, J. P. C. Baena et al., Interpretation and evolution of open-circuit voltage, recombination, ideality factor and subgap defect states during reversible light-soaking and irreversible degradation of perovskite solar cells, *Energy Environ. Sci.* 11 (1) (2018) 151–165. doi:10.1039/C7EE02415K.
- [105] Y. LeCun, Y. Bengio, G. Hinton, Deep learning, *Nature* 521 (7553) (2015) 436–444. doi:10.1038/nature14539.
- [106] Z. Li, F. Liu, W. Yang, S. Peng, J. Zhou, A Survey of Convolutional Neural Networks: Analysis, Applications, and Prospects, *IEEE Transactions on Neural Networks and Learning Systems* 33 (12) (2022) 6999–7019. doi:10.1109/TNNLS.2021.3084827.
- [107] F. Murtagh, Multilayer perceptrons for classification and regression, *Neurocomputing* 2 (5) (1991) 183–197. doi:10.1016/0925-2312(91)90023-5.
- [108] P. S. Efraimidis, P. G. Spirakis, Weighted random sampling with a reservoir, *Information Processing Letters* 97 (5) (2006) 181–185. doi:10.1016/j.ip1.2005.11.003.
- [109] A. Paszke, S. Gross, F. Massa, A. Lerer, J. Bradbury, G. Chanan et al., PyTorch: An Imperative Style, High-Performance Deep Learning Library, in: *Advances in Neural Information Processing Systems*, Vol. 32, Curran Associates, Inc., 2019.
- [110] O. Fischer, A. D. Bui, F. Schindler, D. Macdonald, S. W. Glunz, H. T. Nguyen et al., Versatile implied open-circuit voltage imaging method and its application in monolithic tandem solar cells, *Progress in Photovoltaics: Research and Applications* 33 (1) (2025) 40–53. doi:10.1002/pip.3754.
- [111] L. Wagner, P. Schygulla, J. P. Herterich, M. Elshamy, D. Bogachuk, S. Zouhair et al., Revealing fundamentals of charge extraction in photovoltaic devices through potentiostatic photoluminescence imaging, *Matter* 5 (7) (2022) 2352–2364. doi:10.1016/j.matt.2022.05.024.
- [112] Z. Hameiri, A. Mahboubi Soufiani, M. K. Juhl, L. Jiang, F. Huang, Y.-B. Cheng et al., Photoluminescence and electroluminescence imaging of perovskite solar cells, *Progress in Photovoltaics: Research and Applications* 23 (12) (2015) 1697–1705. doi:10.1002/pip.2716.
- [113] M. Casini, P. De Angelis, E. Chiavazzo, L. Bergamasco, Current trends on the use of deep learning methods for image analysis in energy applications, *Energy and AI* 15 (2024) 100330. doi:10.1016/j.egyai.2023.100330.

Supplementary Information

Quantifying Perovskite Solar Cell Degradation via Machine Learning from Spatially Resolved Multimodal Luminescence Time Series

Giulio Barletta^{1,†}, Simon Ternes^{2,†}, Saif Ali², Zohair Abbas², Chiara Ostendi², Marialucia D'Addio², Erica Magliano², Pietro Asinari^{1,3}, Eliodoro Chiavazzo^{1,*}, Aldo Di Carlo^{2,4,**}

¹Department of Energy, Politecnico di Torino, Corso Duca degli Abruzzi, 24, Torino, 10129, Italy

²CHOSE—Centre for Hybrid and Organic Solar Energy, University of Rome Tor Vergata, Via del Politecnico, 1, Rome, 00133, Italy

³INRIM, Istituto Nazionale di Ricerca Metrologica, Strada delle Cacce, 91, Torino, 10135, Italy

⁴ISM-CNR, Institute of Structure of Matter, Consiglio Nazionale delle Ricerche, Via Fosso del Cavaliere, 100, Rome, 00133, Italy

S1. Measured LED Spectra

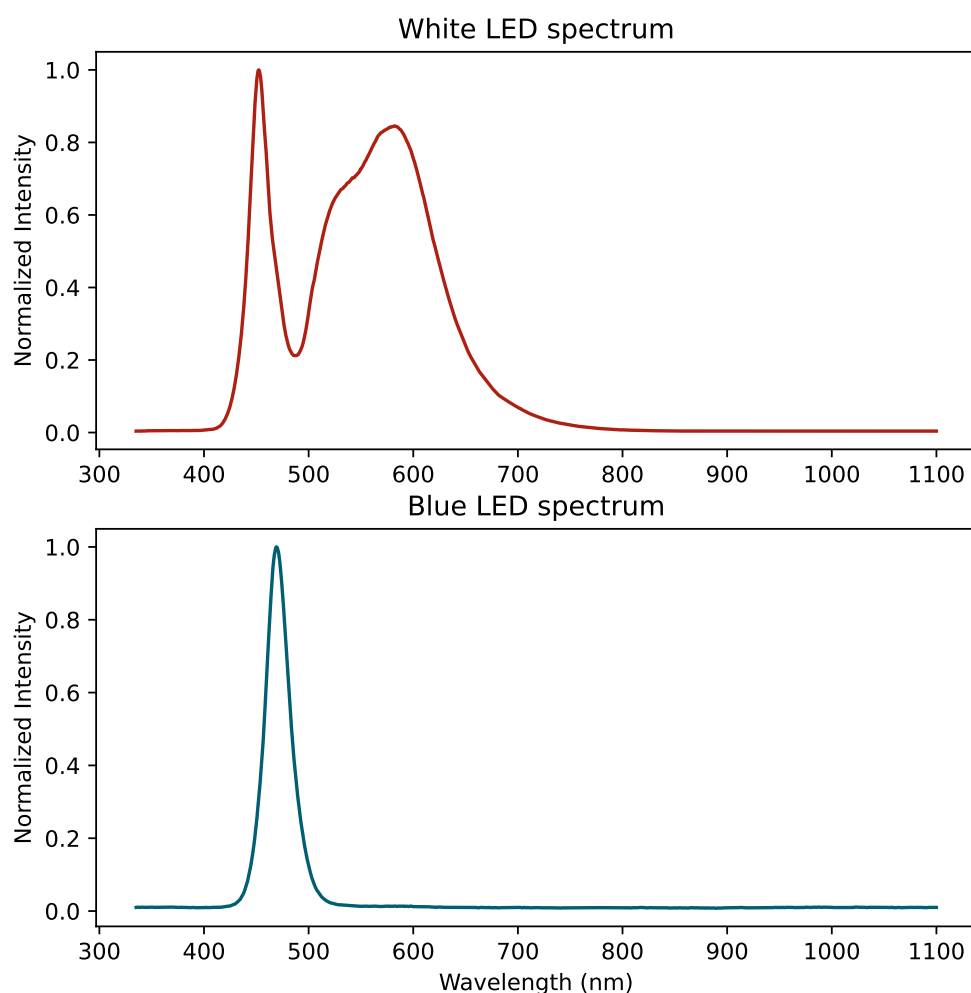


Figure S1: Measured emission spectra of the illumination sources used in the proposed platform. Top: broadband white LED employed for indoor current–voltage (J–V) characterization. Bottom: blue LED used for photoluminescence (PL) excitation. Spectra are shown as normalized intensity versus wavelength.

S2. Custom-built Setup

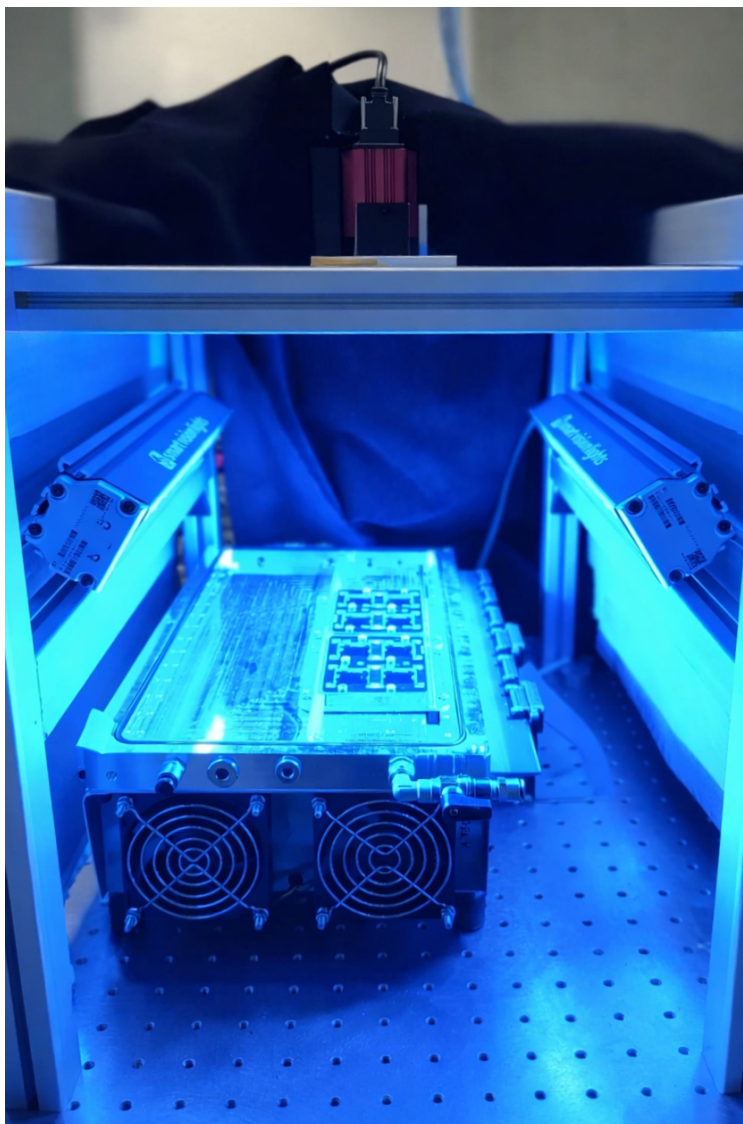


Figure S2: Photograph of the custom-built acquisition rig. The perovskite solar cells are housed in a temperature-controlled measurement chamber mounted on an optical table and electrically contacted for biasing and J–V acquisition. A single sCMOS camera is positioned directly above the measurement plane, with the lens axis normal to the samples plane, and images are acquired through an aperture in the white-LED illumination panel. Two blue LEDs are mounted laterally on the rig and tilted toward the devices, so that the active areas lie within the region of maximum excitation intensity during PL acquisition.

S3. Neural Network Architecture

LumPerNet is a lightweight convolutional regressor that maps time-evolving multimodal luminescence tensors to a scalar efficiency retention (R_{PCE}) target. The model comprises (i) a CNN backbone (TinyBackbone) that extracts a compact global representation from the input image stack, (ii) an optional categorical embedding branch (TabularBranch) encoding the device batch identifier, and (iii) a shallow fully connected prediction head. Unless otherwise stated, LumPerNet outputs a single scalar regression target.

The image input is a tensor $\mathbf{x}_{\text{img}} \in \mathbb{R}^{B \times C \times H \times W}$ where B is the batch size and C is the number of input channels (default $C = 9$ in the implementation). The batch identifier is provided as an integer tensor $\mathbf{s} \in \{0, \dots, N_{\text{batches}} - 1\}^B$.

The image branch is a compact CNN with two convolutional stages and global pooling:

1. Conv2D: $C \rightarrow 16$, kernel 3×3 , padding 1
ReLU activation, Dropout2D ($p = 0.2$), MaxPool2D (2×2)
2. Conv2D: $16 \rightarrow 32$, kernel 3×3 , padding 1
ReLU activation, Dropout2D ($p = 0.2$), MaxPool2D (2×2)
3. AdaptiveAvgPool2D (1×1).

The resulting feature map is globally pooled and flattened to a vector $\mathbf{f}_{\text{img}} \in \mathbb{R}^{B \times 32}$.

Optionally, LumPerNet concatenates the CNN features with a learned embedding of the device batch identifier:

1. Embedding: $N_{\text{batches}} \rightarrow 2$
2. Dropout ($p = 0.1$) applied to the embedding output.

This yields $\mathbf{f}_{\text{tab}} \in \mathbb{R}^{B \times 2}$. The fused representation is $\mathbf{f} = [\mathbf{f}_{\text{img}}, \mathbf{f}_{\text{tab}}] \in \mathbb{R}^{B \times 34}$. If the embedding branch is disabled, the fused vector is simply $\mathbf{f} = \mathbf{f}_{\text{img}} \in \mathbb{R}^{B \times 32}$.

The prediction head is a two-layer MLP:

1. Linear: $\dim(\mathbf{f}) \rightarrow 32$
ReLU activation, Dropout ($p = 0.2$)
2. Linear: $32 \rightarrow N_{\text{targets}}$.

The forward pass returns a dictionary mapping each target name to its corresponding output component.

Unless otherwise stated, ablation variants retain the same CNN backbone and regression head as the base LumPerNet. In the main-text configuration the TabularBranch is disabled, while the ablation study evaluates the effect of enabling the embedding branch.

S3.1. Baseline regressor architecture

To benchmark the contribution of spatial information, we consider a lightweight baseline regressor (BaselineMLP) that operates on the same multimodal inputs as LumPerNet but discards image structure. The baseline first reduces each input channel to a single scalar by spatial averaging over the region of interest, then maps the resulting vector to the R_{PCE} target via a shallow MLP.

Given an image tensor $\mathbf{x}_{\text{img}} \in \mathbb{R}^{B \times C \times H \times W}$, the baseline computes the per-channel spatial mean

$$\mathbf{x}_{\text{img,avg}} = \frac{1}{HW} \sum_{h=1}^H \sum_{w=1}^W \mathbf{x}_{\text{img}}[:, :, h, w] \in \mathbb{R}^{B \times C}, \quad (\text{S1})$$

thereby retaining only global intensity information per channel while removing all spatial features.

Analogously to LumPerNet, the baseline can optionally concatenate a learned embedding of the device batch identifier using the same TabularBranch module (see Section ??). If enabled, the pooled vector is fused as $\mathbf{x} = [\mathbf{x}_{\text{img,avg}}, \mathbf{f}_{\text{tab}}] \in \mathbb{R}^{B \times (C+2)}$. If disabled, the baseline uses only $\mathbf{x} = \mathbf{x}_{\text{img,avg}} \in \mathbb{R}^{B \times C}$.

The fused feature vector is passed to a shallow MLP:

1. Linear: $\dim(\mathbf{x}) \rightarrow 64$
ReLU activation
2. Linear: $64 \rightarrow 32$
ReLU activation
3. Linear: $32 \rightarrow N_{\text{targets}}$.

As in LumPerNet, the model returns a dictionary of outputs, with the primary regression target being the R_{PCE} .

S4. Training and Evaluation Protocol

All models were trained and evaluated under a device-level protocol designed to prevent information leakage across timepoints. The set of per-device files was first split into a training–validation subset ($\sim 80\%$ of total samples) and an independent held-out test subset ($\sim 20\%$ of total samples) using a stratified split with respect to the device batch identifier. All samples originating from the same device were assigned exclusively to a single subset.

Within the training–validation subset, four-fold cross-validation is performed via a stratified K-fold partitioning by device batch ID. For fold k , the k -th fold is used for validation and the remaining folds for training. The same train/validation/test partitions are reused for LumPerNet and the baseline regressor. Reported metrics correspond to the mean \pm standard deviation of held-out test performance across folds.

For each fold, per-channel normalization statistics are computed on the training split only and then applied unchanged to validation and test.

Training batches are drawn using PyTorch’s `WeightedRandomSampler` to mitigate target imbalance within the selected R_{PCE} window. Specifically, the training targets are binned into 20 uniform R_{PCE} bins in $[R_{\text{PCE},\text{min}}, R_{\text{PCE},\text{max}}] = [0.8, 1.2]$; each sample is assigned a weight $w_i \propto 1/n_b$, where n_b is the population of its bin, and sampling is performed with replacement (invalid targets are assigned weight 0). During training only, light geometric augmentation was applied to the multi-channel image tensor using a single random affine transform shared across channels to preserve inter-modality spatial alignment. Augmentations consisted of small random translations (up to ± 2 pixels) and small rotations (up to $\pm 2^\circ$), implemented via affine warping and bilinear resampling. No augmentation was applied during validation or testing.

Unless otherwise stated, models were trained for 100 epochs with batch size $B = 32$ using AdamW (learning rate $\eta = 3 \times 10^{-4}$, weight decay $\beta = 10^{-4}$) and a cosine annealing learning-rate schedule ($T_{\text{max}} = 100$). Early stopping was applied on validation MAE with patience = 50.

S5. Models' performance

S5.1. LumPerNet

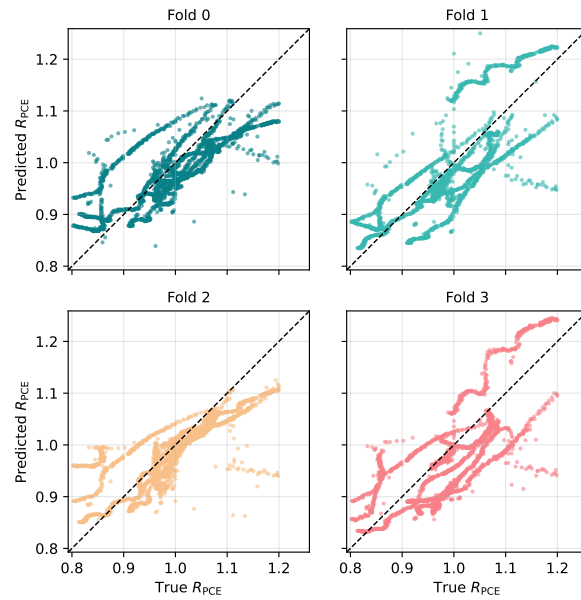


Figure S3: Per-fold parity plots for LumPerNet on the fixed held-out test set. Each panel reports predictions from one fold-specific model trained within the training–validation subset (four-fold CV) and evaluated on the same device-disjoint test set. The dashed black line indicates the identity $\hat{y} = y$.

S5.2. Baseline regressor

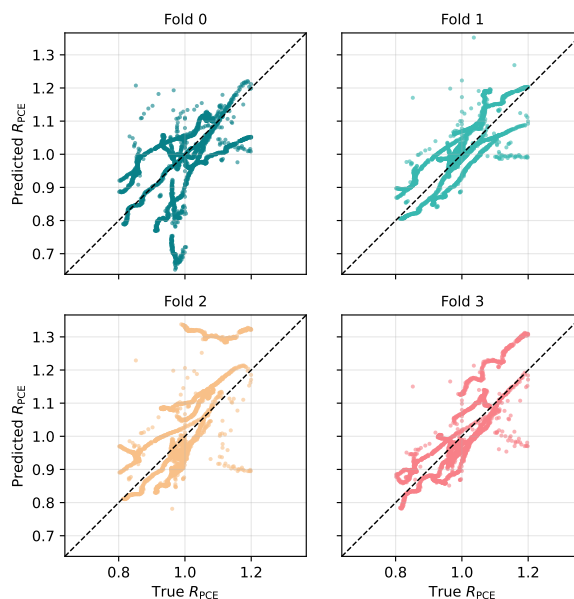


Figure S4: Per-fold parity plots for the `BaselineMLP` models on the fixed held-out test set. Each panel reports predictions from one fold-specific model trained within the training–validation subset (four-fold CV) and evaluated on the same device-disjoint test set. The dashed black line indicates the identity $\hat{y} = y$.

Table S1: Per-fold performance of the `BaselineMLP` models on the validation and held-out test sets (R_{PCE} prediction). Reported values are computed independently for each fold; the last row summarizes the mean \pm standard deviation across folds. Each fold denotes one cross-validation training run performed on the device-level training–validation subset; the held-out test set contains disjoint devices and is identical across folds.

Fold	Validation			Test (held-out)		
	MAE ↓	RMSE ↓	R^2 ↑	MAE ↓	RMSE ↓	R^2 ↑
0	0.050	0.072	0.246	0.076	0.101	-0.213
1	0.084	0.106	-0.044	0.047	0.057	0.611
2	0.087	0.122	-0.291	0.081	0.106	-0.346
3	0.039	0.053	0.669	0.052	0.065	0.490
$\mu \pm \sigma$	0.065 ± 0.021	0.088 ± 0.027	0.145 ± 0.357	0.064 ± 0.015	0.082 ± 0.021	0.136 ± 0.420

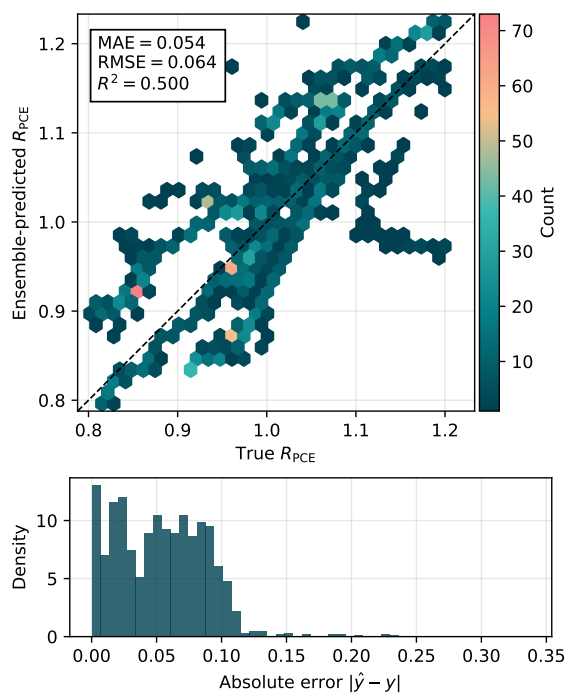


Figure S5: Baseline regressor ensemble-mean parity plot and absolute error distribution for R_{PCE} prediction on the held-out test set. Top: hexbin parity plot comparing measured R_{PCE} to the ensemble-mean prediction \hat{y} , computed by averaging the outputs of the four CV-trained `BaselineMLP` models (one prediction per test sample). Color denotes the number of samples per bin, and the dashed line indicates the ideal $\hat{y} = y$ relationship; inset reports the corresponding ensemble performance metrics. Metrics shown in the inset are computed on the ensemble-mean predictor (mean of the 4 fold-trained models) evaluated on the held-out test set, whereas Table S1 reports mean \pm std across fold-wise test evaluations. Bottom: distribution of absolute residuals $|\hat{y} - y|$ over the held-out test samples, summarizing the typical magnitude and spread of prediction errors within the operational range $R_{PCE} \in [0.8, 1.2]$.

S5.3. Ablation study — multi-modality importance

Table S2: Per-fold performance of the LumPerNet models under single-modality ablations on the validation and held-out test sets (R_{PCE} prediction). Reported values are computed independently for each fold; the last row summarizes the mean \pm standard deviation across folds. Each fold denotes one cross-validation training run performed on the device-level training-validation subset; the held-out test set contains disjoint devices and is identical across folds.

Modality	Fold	Validation			Test (held-out)		
		MAE \downarrow	RMSE \downarrow	R^2 \uparrow	MAE \downarrow	RMSE \downarrow	R^2 \uparrow
EL	0	0.049	0.064	0.406	0.065	0.081	0.215
	1	0.069	0.087	0.291	0.051	0.066	0.473
	2	0.104	0.132	-0.521	0.067	0.078	0.261
	3	0.070	0.084	0.169	0.060	0.075	0.321
	$\mu \pm \sigma$	0.073 ± 0.020	0.092 ± 0.025	0.096 ± 0.361	0.061 ± 0.006	0.075 ± 0.006	0.317 ± 0.098
PL _{oc}	0	0.055	0.068	0.342	0.062	0.076	0.312
	1	0.071	0.086	0.314	0.055	0.070	0.406
	2	0.093	0.108	-0.024	0.062	0.076	0.307
	3	0.051	0.064	0.521	0.069	0.085	0.124
	$\mu \pm \sigma$	0.067 ± 0.017	0.081 ± 0.018	0.288 ± 0.197	0.062 ± 0.005	0.077 ± 0.005	0.287 ± 0.102
PL _{sc}	0	0.053	0.069	0.306	0.062	0.077	0.284
	1	0.087	0.105	-0.024	0.061	0.073	0.363
	2	0.085	0.108	-0.024	0.075	0.101	-0.237
	3	0.046	0.058	0.602	0.053	0.068	0.450
	$\mu \pm \sigma$	0.068 ± 0.019	0.085 ± 0.022	0.215 ± 0.261	0.063 ± 0.008	0.080 ± 0.013	0.215 ± 0.267
EL+PL _{oc}	0	0.039	0.048	0.674	0.065	0.079	0.245
	1	0.068	0.087	0.292	0.063	0.092	-0.019
	2	0.087	0.107	0.000	0.061	0.076	0.303
	3	0.051	0.069	0.444	0.051	0.068	0.450
	$\mu \pm \sigma$	0.061 ± 0.018	0.078 ± 0.022	0.352 ± 0.245	0.060 ± 0.005	0.079 ± 0.009	0.245 ± 0.170
EL+PL _{sc}	0	0.048	0.058	0.521	0.054	0.064	0.510
	1	0.081	0.098	0.110	0.054	0.066	0.480
	2	0.094	0.118	-0.213	0.052	0.062	0.543
	3	0.045	0.058	0.606	0.050	0.060	0.572
	$\mu \pm \sigma$	0.067 ± 0.021	0.083 ± 0.026	0.256 ± 0.329	0.052 ± 0.002	0.063 ± 0.002	0.526 ± 0.034
PL _{oc} +PL _{sc}	0	0.046	0.065	0.401	0.058	0.070	0.410
	1	0.061	0.075	0.467	0.054	0.069	0.428
	2	0.085	0.102	0.101	0.042	0.061	0.550
	3	0.038	0.052	0.682	0.052	0.067	0.457
	$\mu \pm \sigma$	0.057 ± 0.018	0.073 ± 0.018	0.413 ± 0.208	0.051 ± 0.006	0.067 ± 0.003	0.461 ± 0.054

S5.4. Ablation study — batch identity importance

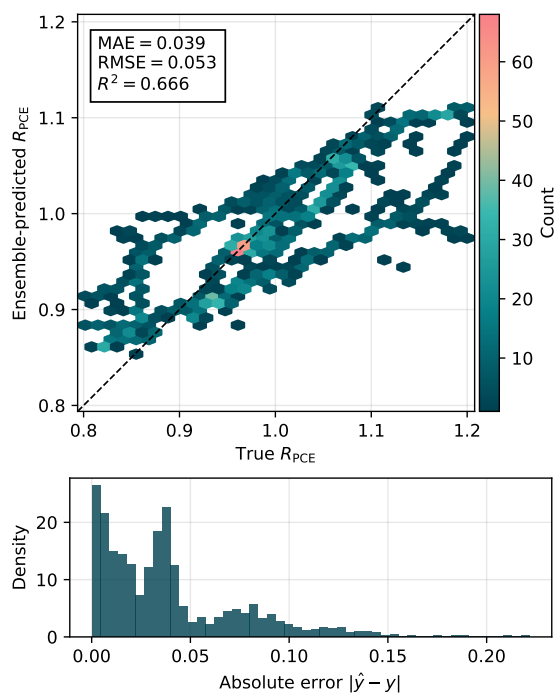


Figure S6: LumPerNet+ (LumPerNet with enabled TabularBranch) ensemble-mean parity plot and absolute error distribution for R_{PCE} prediction on the held-out test set. Top: hexbin parity plot comparing measured R_{PCE} to the ensemble-mean prediction \hat{y} , computed by averaging the outputs of the four CV-trained LumPerNet+ models (one prediction per test sample). Color denotes the number of samples per bin, and the dashed line indicates the ideal $\hat{y} = y$ relationship; inset reports the corresponding ensemble performance metrics. Bottom: distribution of absolute residuals $|\hat{y} - y|$ over the held-out test samples, summarizing the typical magnitude and spread of prediction errors within the operational range $R_{\text{PCE}} \in [0.8, 1.2]$.

Table S3: Per-fold performance of the LumPerNet+ models on the validation and held-out test sets (R_{PCE} prediction). Reported values are computed independently for each fold; the last row summarizes the mean \pm standard deviation across folds. Each fold denotes one cross-validation training run performed on the device-level training-validation subset; the held-out test set contains disjoint devices and is identical across folds.

Fold	Validation			Test (held-out)		
	MAE ↓	RMSE ↓	R^2 ↑	MAE ↓	RMSE ↓	R^2 ↑
0	0.043	0.061	0.468	0.050	0.062	0.538
1	0.077	0.091	0.220	0.052	0.072	0.380
2	0.084	0.106	0.018	0.037	0.051	0.684
3	0.040	0.049	0.711	0.043	0.057	0.615
$\mu \pm \sigma$	0.061 ± 0.019	0.077 ± 0.023	0.354 ± 0.260	0.045 ± 0.006	0.060 ± 0.008	0.554 ± 0.113

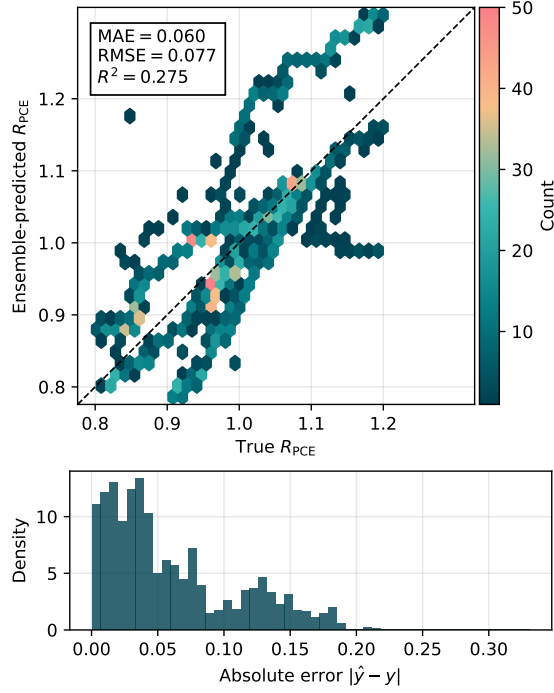


Figure S7: **BaselineMLP+** (**BaselineMLP** with enabled **TabularBranch**) ensemble-mean parity plot and absolute error distribution for R_{PCE} prediction on the held-out test set. Top: hexbin parity plot comparing measured R_{PCE} to the ensemble-mean prediction \hat{y} , computed by averaging the outputs of the four CV-trained **BaselineMLP+** models (one prediction per test sample). Color denotes the number of samples per bin, and the dashed line indicates the ideal $\hat{y} = y$ relationship; inset reports the corresponding ensemble performance metrics. Bottom: distribution of absolute residuals $|\hat{y} - y|$ over the held-out test samples, summarizing the typical magnitude and spread of prediction errors within the operational range $R_{\text{PCE}} \in [0.8, 1.2]$.

Table S4: Per-fold performance of the **BaselineMLP+** models on the validation and held-out test sets (R_{PCE} prediction). Reported values are computed independently for each fold; the last row summarizes the mean \pm standard deviation across folds. Each fold denotes one cross-validation training run performed on the device-level training-validation subset; the held-out test set contains disjoint devices and is identical across folds.

Fold	Validation			Test (held-out)		
	MAE \downarrow	RMSE \downarrow	R^2 \uparrow	MAE \downarrow	RMSE \downarrow	R^2 \uparrow
0	0.045	0.069	0.315	0.058	0.069	0.431
1	0.112	0.136	-0.744	0.101	0.120	-0.722
2	0.081	0.113	-0.119	0.063	0.083	0.182
3	0.059	0.071	0.405	0.069	0.090	0.038
$\mu \pm \sigma$	0.074 ± 0.025	0.097 ± 0.029	-0.035 ± 0.454	0.073 ± 0.017	0.090 ± 0.019	-0.018 ± 0.430